Energy Conversion and Management 294 (2023) 117520

Contents lists available at ScienceDirect

Energy Conversion and Management

journal homepage: www.elsevier.com/locate/enconman

Power-to-methane via co-electrolysis of H_2O and CO_2: Reactor operation and system simulation

Philippe Aubin [a], Ligang Wang [b,c,*], Jan Van herle [a]

[a] Group of Energy Materials, Swiss Federal Institute of Technology in Lausanne, Switzerland
[b] Institute of Energy Power Innovation, North China Electric Power University, China
[c] Key Laboratory of Power Station Energy Transfer Conversion and System (North China Electric Power University), Ministry of Education, China

ARTICLE INFO

Keywords:
Power-to-methane
Solid-oxide electrolyzer
Co-electrolysis
Syngas methanation
System simulation

ABSTRACT

The traditional pathway of electrolysis based power-to-methane systems consists of water (liquid or vapor) electrolysis followed by CO_2 methanation. The use of solid-oxide electrolysers allows an alternative pathway, i.e., steam and CO_2 electrolysis followed by syngas methanation which can be more efficient than the traditional pathway but requires additional considerations related to cost and operation. The operation of an evaporating water-cooled CO_2 methanation reactor in syngas methanation is first validated: (1) H_2 concentrations between 10.3 and 21.0 % are measured with the lowest concentration occurring at higher reactant pressure and cooling water pressure and lowest reactant flow rate. (2) Increasing the CO concentration in the reactant, while supplying the stochiometric ratio of H_2 and a ratio of H_2O to CO of 1, increases the measured hot spot temperature but it remains under 700 °C. However, the changes in H_2 concentration at the outlet are within the error of the injected reactant.

Furthermore, an idealized power-to-methane system is analyzed, using various system layouts, to identify the impact of the steam production's energy source, as well as the additional steam requirement for syngas methanation, on the system's heating value efficiency and on the key operating variables. Restricting the internal steam production to the cooling system of the reactor causes a decrease in maximum efficiency from 94.1% to 91.1%. Directly compressing the humid mixture to be injected into the reactor as it exits the solid-oxide electrolyzer partially alleviates the stress of restricting the evaporation process to reach a maximum efficiency of 92.4%. When including heat losses in the reactor, avoiding the condensation offered a gain of up to 1.2% compared to condensing the water before the compression step.

1. Introduction

Since the discovery of the Sabatier reaction in 1902, the work related to methanation has been focused primarily on CO methanation for the gas cleaning in ammonia and hydrogen production [1–3]. The development of CO_2 methanation was a by-product of the work on CO methanation. The development of syngas methanation is motivated by the solid-to-gas pathways such as biomass gasification followed by syngas methanation [4]. However, as presented theoretically by Wang et al. [5], a solid oxide electrolyzer (SOE) in co-electrolysis followed by syngas methanation (Eqs. (1) & (2)) is an alternative Power-to-methane (PtM) with higher peak theoretical efficiency compared to the steam electrolysis-CO_2 methanation pathway. Given the reversibility of the SOE, the possibility of using CH_4 directly in the same system but in fuel cell mode, and the high theoretical electrical [6] and co-generation two-way efficiencies, this technology is a valid alternative to batteries for seasonal storage of renewable electricity. Mebrahtu et al. [7] tested the concept of coupling a SOE in steam and CO_2 co-electrolysis operation by performing syngas methanation in a reactor using ratios of CO_2 and CO, which could be obtained using the SOE based on their co-electrolysis experimental results. Their methanation experiment was completed on Ni-Fe/(Mg,Al)Ox and commercial Ni/AlO_3 catalysts.

$$CO_2(g) + 4H_2(g) \rightarrow CH_4(g) + 2H_2O(g),\ \Delta H(298\,K) = -165\,kJ/mol \quad (1)$$

$$CO(g) + 3H_2(g) \rightarrow CH_4(g) + H_2O(g),\ \Delta H(298\,K) = -206\,kJ/mol \quad (2)$$

$$CO_2(g) + H_2(g) \rightarrow CO(g) + H_2O(g),\ \Delta H(298\,K) = 41\,kJ/mol \quad (3)$$

According to Gao et al. [8], the methanation of CO_2 would consist of the Reverse-Water-Gas-Shift followed by the methanation of CO: many authors support this theory [9–12]. Other researchers, however, propose pathways through which, for example, carbonates and formate

* Correspondence to: Institute of Energy Power Innovation, North China Electric Power University, China.
E-mail addresses: philippe.aubin@epfl.ch (P. Aubin), ligang.wang@ncepu.edu.cn (L. Wang).

https://doi.org/10.1016/j.enconman.2023.117520
Received 19 April 2023; Received in revised form 25 July 2023; Accepted 8 August 2023
Available online 4 September 2023

species are intermediary steps. Lately, the development of in-operando DRIFT allowed further insight into reaction pathways; depending on the catalyst, support and preparation method both paths were observed [13,14]. Takano et al. [15], who presented a precursor version of the catalyst used in this study, proposed the CO_2 methanation to occur through a carbonate-formate pathway. This selection was based on previous measurements (Fourier-transform infrared spectroscopy and Temperature-programmed desorption), performed by others [16–19] on various crystal formations of ZrO_2 supported Ni. More measurements have been performed since these publications that support the formate pathway [14,20] for Ni/ZrO_2 catalyst with both monoclinic and tetragonal lattices manufactured by calcination. However, the proposed pathway avoids the carbonate formation by making the CO_2 bind to a hydroxide group on the support instead of a vacancy and oxide pair. Conversely, the formate species could be spectators [21] or even an intermediary step to the formation of CO [22].

In the case of syngas methanation, the presence of CO at the inlet results in the three reactions occurring in the reactor independently of the CO_2 methanation pathway. The outlet reactor composition is the summation of the kinetics of each reaction as a function of temperature and pressure. The relative kinetic of CO methanation vs. CO_2 methanation is dependent on the catalyst, the support, the promoters, the preparation method and the operating conditions [9,16,22–24]; the CO_2 methanation can be more reactive under certain conditions [16,25]. According to the work by Le et al. [26], CO methanation is more reactive than CO_2 methanation on Ni/ZrO_2 while the opposite occurs with Ni/CeO_2, the latter trend being caused by high levels of CO_2 adsorption even at low temperatures using CeO_2. Furthermore, CO_2 methanation is not favored while there is still CO available [1,11, 22,25], even with 30 ppm CO at 227 °C on Ni/SiO_2 [11], which was simulated using microkinetic modeling by Schmider et al. [22]. Also, the CO_2 concentration increased through the WGS reaction until the complete conversion of CO.

The methanation of CO presents a greater risk of catalyst deactivation compared to CO_2 methanation. The higher exothermicity of CO methanation intensifies the risk of sintering due to higher hot spot. The stochiometric feed of CO methanation has lower ratios of H/C and O/C resulting in greater risk of carbon deposition at lower temperatures (450–700 °C) through reactions such as the Boudouard reaction as identified by the thermodynamic analysis by Gao et al. [8]. Gao et al. analyzed CO and CO_2 methanation by calculating the equilibrium concentrations as a function of temperature, pressure, stochiometric ratio and added steam content. In the thermodynamic analysis, the carbon formed was assumed as a condensed specie. A more detailed analysis of C-H-O ratios to form carbon deposits for various temperatures and pressures was presented by Jaworski and Pianko-Oprych [27]. The authors identified that the effect of pressure was dependent on the composition. For that reason, Gao et al. [8] identified the opposite effect of pressure when focusing on methanation compositions (4 H_2:CO_2 and 3H_2:CO). In Fig. 1, the case of CO methanation with and without steam shows the former outside the carbon deposition region for temperatures between 450 to 700 °C. However, McCarty and Wise identified carbon formation at lower temperatures even though it is thermodynamically unfavored [28,29]. Regarding the kinetics of carbon deposition, Ni is prone to carbon deposition, but the support being composed of ZrO_2 can decrease the rate of carbon deposition [14,30,31]. In addition, at low temperature and with high CO concentration, certain metal catalysts, such as Ni, will produce carbonyl species causing the loss of catalyst with the metal leaving in the gas phase or deactivation through 'smoothing' and sintering [28,32].

The internal reforming capabilities of solid-oxide cells (SOC) in fuel cell mode are exploited in commercial units. However, the reverse reaction, production of methane internally, is still limited to a research level unit even though this capability has been known for over a decade. While varying the methane concentration in their internal reforming experiment, Timmermann et al. [33] identified a

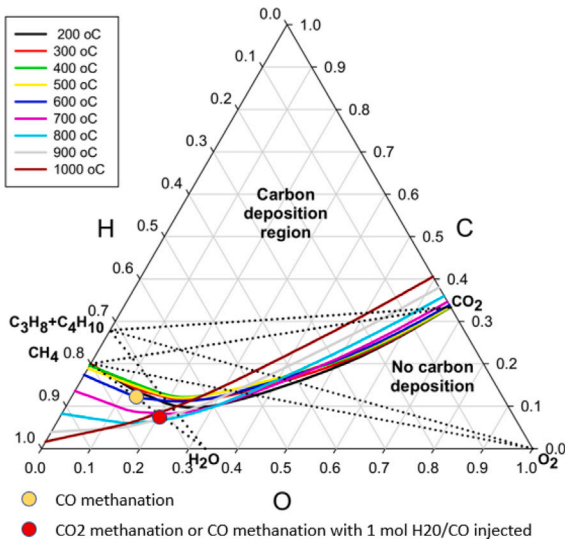

Fig. 1. Ternary diagram for 30 bar A. *Source:* Modified from Jaworski et al. [27].

net production of methane at low methane inlet concentration and low temperature (650 °C) rather than a net reforming. Furthermore, the outlet concentration followed the thermodynamic equilibrium indicating that the operating conditions (pressure and temperature) are the limiting factor rather than the kinetics at the current operating conditions and flow rates. Internal methanation occurs in the SOE in the presence of hydrogen and carbon in the form of CO_2 and CO, with the highest rate of reaction occurring with CO. During co-electrolysis of steam and CO_2, internal methanation is promoted from the formation of hydrogen though the electrochemical dissociation of H_2O and the formation of CO from both the electrochemical dissociation of CO_2 and the chemical transformation resulting from the reverse-water-gas-shift reaction. Nevertheless, internal methanation increases the internal heat generation, and thus, a new method to extract heat might be needed such as the one presented by Zeng et al. [34] who implemented high temperature heat pipes in a solid-oxide fuel cell (SOFC).

Increasing the pressure while decreasing the temperature improves the methane equilibrium concentration. Consequently, lowering the temperature and pressurizing the stack are required to reach sufficient level of internal methanation for practical uses. Biswas et al. [35] provided a detailed review on materials, geometry etc. of methane production including through SOE based systems. The authors completed their review with a high level comparison of estimated system efficiencies of five pathways and concluded that the case of high temperature co-electrolysis with internal methanation had the highest potential efficiency. Xiufu et al. performed a thermodynamic analysis of the direct synthesis of methane and dimethyl ether inside a SOE [36]. The authors propose operating at higher temperature to avoid carbon formation which is further promoted on Ni catalyst.

Steam electrolysis and co-electrolysis of steam and CO_2 under pressurized operation has been investigated experimentally at high temperature on single cells at 800 °C [37,38] and on stacks [39–41]. On the single cell level, Bernadet et al. tested Ni-YSZ/YSZ/CGO-LSCF cells between 1 and 10 bar A. In both modes, the increase in pressure resulted in an increase in the OCV, but a decrease in concentration overpotential; increasing the limiting current. The authors hypothesized that the relationship is due to the improvement in mass diffusion with pressure. What is not mentioned is the increase in the current in co-electrolysis due to internal methanation, making higher amounts of O^{2-} anion available for transport. The measurements were used to develop two versions of a code that uses kinetic models to estimate

the rate of various reactions. Yet, the co-electrolysis version of the code underestimates the methane production. Furthermore, the code was used to develop an operating map for a fixed cell voltage and a constant pressure of 1.3 V and 10 bar A, respectively, while varying the temperature between 700 °C and 800 °C. Their analysis was limited to above 700 °C to avoid carbon deposition which is thermodynamically favored under this limit, depending on the flow composition. During the experiment in co-electrolysis mode, and in the related operating map, the methane dry gas composition at the outlet was limited (< 8%) due to such high temperatures. With higher over-voltage, their simulation limited the methane formation at lower temperatures by the use of constant voltage, leading to lower the current density.

On the stack level, Jensen et al. [39] performed a reversible operation of a pressurized solid-oxide 30 cells stack at 700 °C. An initial characterization of the stack was performed in both steam electrolysis and fuel cell modes with 50%/50%, the pressure was increased to 18.7 bar A in multiple steps, and for each, IV and EIS measurements were taken. Similarly to Bernadet et al.'s observation, with pressurization, the OCV voltage increases and the polarization resistance decreases. However, the EIS spectrum shifts towards the lower frequency indicating a worsening of the ohmic resistance, contradicting the results from Wu and Shy [42], and the authors' justification is a possible loss in contact. A significant quantity of air was then found to be leaking into the fuel side, and with post-test SEM imaging indicating contact losses, cracks in the electrolyte and the oxygen electrode, delamination and oxidation of the fuel electrode, the remainder of the test is questionable. On the other hand, Riedel et al. also recorded pressurized performance and durability tests [40,41] of a stack composed of 10 electrolyte supported cells and a stack of 10 electrode supported cells in steam electrolysis, CO_2 electrolysis, and steam and CO_2 co-electrolysis. In their durability test of 1000–2000 h, pressurized operation increased the degradation due to the increase in Ni migration such that the fuel electrodes became slightly insulating. The degradation was worst for co-electrolysis compared to traditional steam electrolysis. The authors, however, mention that the length of the tests are insufficient to state the impact of pressure on long term operation. The CH_4 composition at the outlet of the stack in co-electrolysis mode followed closely the thermodynamic equilibrium. However, as the stacks were operated above 750 °C and with pressures under 8 bar A, the maximum methane concentration of only approximately 7% could be reached. In terms of performance, increasing the pressure improved the fuel electrode supported stack's performance while having a limited impact on the electrolyte supported stack. The improvement of the performance of the electrode supported cells could be due to a decrease in the mass diffusion limitation as hypothesized by Bernadet et al. [37,38] while electrolyte supported cells have lower mass diffusion limitation due to the thinner electrodes. For both stacks, regardless of the pressure, the performance was best for steam electrolysis and worse for CO_2 electrolysis.

Providing the optimal conditions for internal methanation would allow the majority of the methane to be produced inside the SOE. However, the methanation process is not required to occur at the TPB, and even in the electrode. As a consequence, the cell geometry can be modified to maximize catalytic potential without affecting the electrochemical performance. Baxter et al. [43] tested a YSZ electrolyte button cell at 450 °C and improved the CO_2 conversion by a catalyst layer on top of the cathode and inside the outlet tube. However, a ratio of H_2 to H_2O of 4 was fed to compensate for the very low electrochemical performance of the YSZ electrolyte at such low temperatures. Furthermore, some of the CO_2 conversions measured were also inflated by the use of a H_2 to CO_2 feed ratio of up to 11.

Many researchers have simulated cells and stacks under pressurized operation [5,37,38,44–48] as either stand alone units or as part of different systems. A modification to the traditional stack geometry was presented by Chen et al. [46] that simulated a solid-oxide electrolyzer-Fischer–Tropsch (SOE-FT) reactor consisting of a single ceramic cell, but with a negative thermal gradient along the length of the cell. At the inlet, where the temperature is high, an anode electrode is used to perform electrochemical reaction while in the section closer to the lower temperature outlet, no anode is located on the other side of the electrolyte. In the second region, the negative temperature gradient results in methane production being favored. The advantage of this method is the decoupling between cell temperature and methane production compared to internal methanation. The higher temperature region improves the electrochemical performance through limiting the over-voltage resulting in the increase in the methane production due to larger quantity of syngas generated for the same applied voltage. In addition, the required pressure of the system to reach the same level of internal methanation is lowered as the equilibrium conversion increases through the temperature gradient rather than by the pressure. On the other hand, their simulation indicated a saturation of the methane yield happening at roughly 2.7 bar A due to the fixed applied voltage which limited the hydrogen production.

Kazempoor and Braun [48] used their SOEC model to analyze the effect of the ratios of S/C and H_2O/CO_2, inlet temperature and current density on the stack power consumption and outlet compositions. Some of the important conclusions identified by the authors are: (1) the RWGS reaction causes significant dependencies of both outcomes on the operating conditions and (2) CO_2 rich fuel and low S/C increase the power requirement of the stack. The effect of the CO_2 content in the inlet gas is in accordance to the work by Riedel et al. [40].

In a previous work [49], an evaporating water cooled reactor using approx. 1.1 L of packed cylindrical pellets of Ni/ZrO_2 catalyst was developed for CO_2 methanation (Eq. (1)). This reactor is to be coupled to a solid oxide electrolyzer in a power-to-methane (PtM) system under steam electrolysis-CO_2 methanation operation. The alternative co-electrolysis operation of the SOE in the final coupling will be investigated. Consequently, the safe and efficient operation of the reactor in syngas methanation operation must also be validated.

In the experiment by Mebrahtu et al. [7], the micro-reactor was placed inside an oven to maintain a fixed temperature, and thus, the effect on the reactor temperature is limited. In this manuscript, the reactor developed previously [49] is first tested for syngas methanation with varying ratio of $CO/(CO+CO_2)$ to verify the effect of the CO on the hot spot and on the outlet concentrations. The operation included the injection of steam with the reactant with a constant ratio of 1 mole of steam per mole of CO to avoid carbon deposition, and this decision can affect the system's response. Therefore, the impact of the injected steam on the system's performance is investigated. As the PtM system in which the methanation reactor will be used is under development, the effect of the steam can only be assessed through a series of system simulations, building upon the work by Wang et al. [5,6,50,51] that injected dry gas mixtures in their isothermal equilibrium reactor. The effect of the steam injection in the reactor, and of its source, on the performance and operation of the system are examined. The theoretical system layout was also changed to avoid the condensation at the outlet of the SOE, and thus, use the remaining steam to fulfill the requirement at the inlet of the reactor. Further stress is also introduced to the final two system layouts by including the estimated reactor heat losses identified during the experiment. The aim is to assess the impact of the added steam generation, limiting the evaporation process to the reactor's cooling system and heat losses on the overall efficiency and on the operating strategies (optimal operating variables).

The descriptions of the experimental setup and operating conditions of the reactor followed by the system simulation based on the previous works [5,6,49–53] are presented in Sec. 2. In the result section, (Sec. 3), the temperature profile, outlet composition and steam generation are discussed in Section 3.1 while the comparison of the PtM layouts and operating strategies is discussed in Section 3.2.

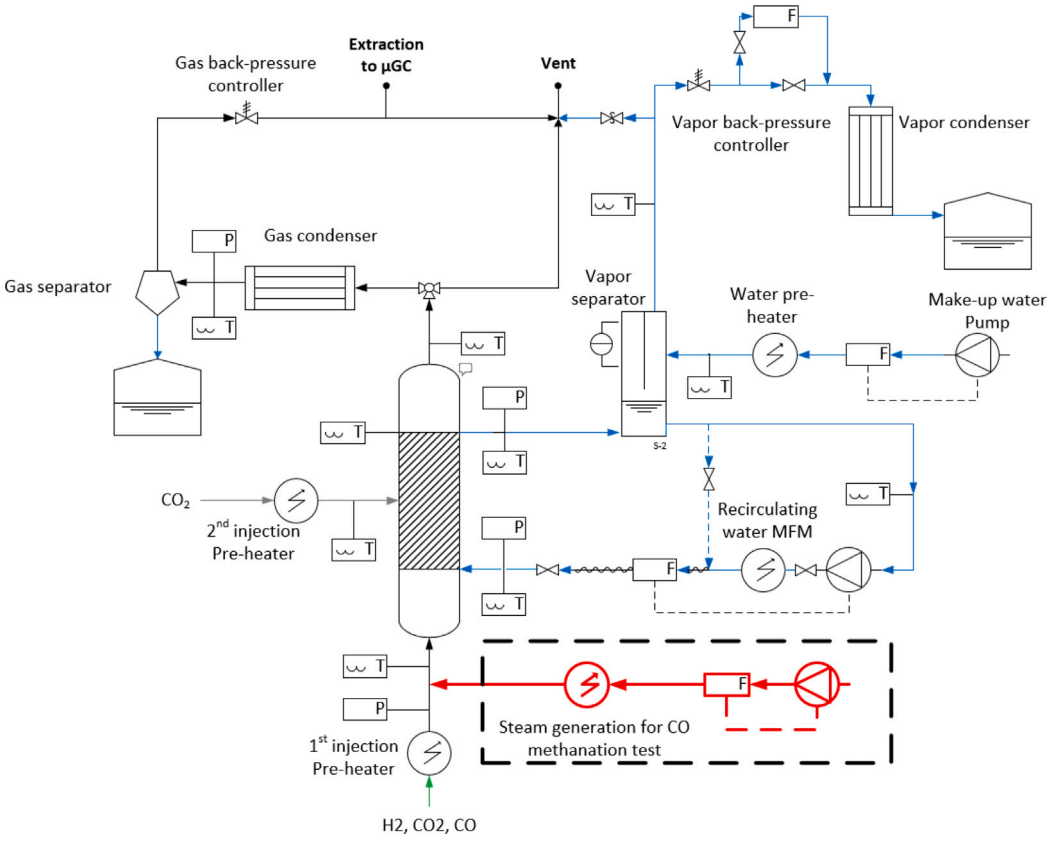

Fig. 2. Simplified schematic of the methanation reactor with BoP, adapted from Aubin et al. [49] to include the evaporator, with permission from Elsevier, copyright 2023.

2. Methodology

2.1. Syngas methanation operation

The system shown in Fig. 2 designed for CO_2 methanation, was introduced by Aubin et al. [49] with a 5–8.5 kW_{HHV} H_2 (in CO_2 methanation operation) reactor and an added evaporator at the inlet. The reactor consists of a concentric shell and tube with the Ni/t-ZrO_2 catalyst pellets located in the central tube. The catalyst bed has a diameter of 31.5 mm and comprises of two reactive sections (0.4 and 1.1 m in lengths) separated by an inert region of 10 cm for a possible second injection of reactant. A 20-measurement multi-point thermocouple is placed along the central axis of the reactor to measure the temperature profile and capture the hot spot.

As the coupling between the SOE and the reactor is under development, the characterization of the reactor is performed using pressurized H_2 and CO_2 bottles with flow rates controlled using mass flow controllers. In addition, the recovery of the heat available at the outlet of the reactor to preheat the reactant has yet to be introduced, and thus, the entirety of the preheating is completed using a helical tube placed inside a radiating oven. At the outlet of the reactor, the product gases are condensed and the water is separated using a pressurized separator with an automatic floater-valve mechanism. The dry-gas concentrations are measured using a microGC 490 from Agilent Technologies®. In the cooling loop, two VGS040 pumps from Verder®are used as a make-up pump and a recirculation pump. Heating the make-up water, the recirculation loop and the vapor line are completed using heating cords. The three flow meters (2 liquid water and 1 vapor) in the water system are Coriolis flow meters from the Promass series of Endress + Hauser®.

The analysis performed by Gao et al. [8] is repeated using the HSC GEM software for CO methanation with three cases of steam content and is presented in Fig. 3. Without steam, carbon formation can be favored inside the reactor if the hot spot reaches above approximately 500 °C. The addition of steam can prevent carbon formation and the H/C/O ratio to be injected should be optimized for the specific reactor as the kinetics of carbon formation depends on the catalyst. However, to ensure that the thermodynamic equilibrium does not favor carbon formation, as presented, a ratio of H_2O /CO of 0.5 should be sufficient to ensure no carbon deposition. In addition, at the outlet of an SOE in co-electrolysis mode, the outlet composition also consists of a significant amount of CO_2, and thus, the gas mixture (before and after condensation) is further from the carbon formation region. Nevertheless, a surplus of steam can be injected to ensure no local carbon formation occurs if the mixture concentration varies spatially.

The manufacturer of the catalyst pellets used in the reactor advises the injection of at least 1 mole of steam per CO, even though the thermodynamic indicates that this solution is excessive. Consequently, with this steam feed, the H/C/O ratio at the inlet of the reactor is the same as CO_2 methanation: thermodynamically, the final state should be the same. However, the injection of CO_2 moves the equilibrium away from carbon formation. Gao et al. [8] also simulated a mixture with a ratio of 1CO:1CO_2 without steam, but with the stochiometric quantity of H_2, and found no carbon deposition at the thermodynamic equilibrium. The steam requirement can vary depending on the mixture generated by the SOE. Therefore, the possible mixtures at the outlet of the SOE must first be identified.

Thermodynamic equilibrium calculations have been used to estimate the outlet concentration of an SOE in co-electrolysis [36,54]. In the limited literature with concentration measurements [7,39,41,55–57], the deviations from the equilibrium vary depending on the operating conditions: current, reactant mixture, cells materials, cells structure, pressure and temperature. However, the deviations are limited as the kinetics of each chemical reaction (WGS, primarily, but also the methanation reactions) at the operating temperature of the SOE are such that they will compensate for the relative level of reduction of CO_2 and H_2O, which also varies with the same parameters listed

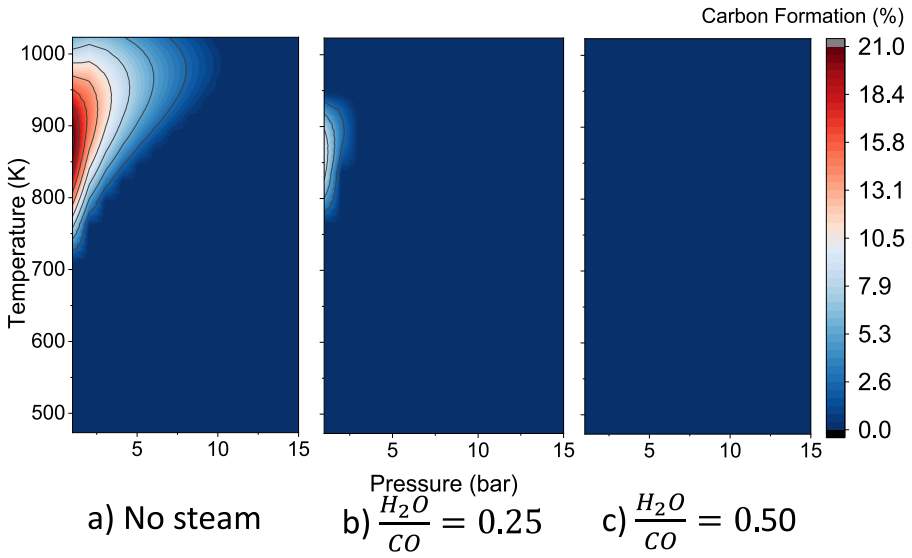

Fig. 3. Carbon formation for CO methanation with varying steam content, extended analysis from Gao et al. [8].

previously. As the concentration measurements are the summations of the electrochemical and chemical reactions, attempts at quantifying the relative contributions of the CO_2 reduction and the RWGS reaction in the production of the CO have been performed [56–59]. Some of the conclusions are: (1) both pathways are present with the RWGS potentially being the primary contributor, (2) the relative contributions are dependent on the cell materials and cell structures, (3) using excess H_2 at the inlet will increase the contribution of the RWGS reaction, and (4) increasing the utilization factor increases the contribution of the direct reduction of the CO_2. Lastly, a large variety of mixtures of CO, CO_2, H_2 and CH_4 can be obtained with a single system by varying the operating conditions [7,36,54,60].

An example of thermodynamic equilibrium concentration as a function of the SOE utilization factor is presented in the supplementary document. Regardless of the production of CO and CH_4, the modular number $(H_2\text{-}CO_2)/(CO+CO_2)$ at the outlet of the SOE should be equal to 3 to satisfy the stoichiometry of the methanation reactions. Therefore, for a specific cell outlet temperature and reactant flow rate, there is only a single utilization at which the modular number is ideal. Additionally, in this example, the carbon deposition is not favored, but depending on the temperature, the pressure, the CO_2 injected and the utilization factor, carbon deposition is a possibility [60]. Also, for the conditions simulated, the quantity of CH_4 that can be produced is limited until a high utilization factor is reached.

With respect to the reactor's response, the carbon deposition at equilibrium in the reactor is also presented in the supplementary document. In this case, the water is separated from the SOE's product before the injection of the dry gases in the reactor, and the ratio of $CO/(CO+CO_2)$ is varied from 0 to 100%. There is a risk of carbon deposition at the hot spot due to local change in composition, and even the possibility of carbon formation outside the range where it is thermodynamically favored [28,29]. In addition, the operation of the reactor with dry gases and at low pressures has high risk of carbon deposition if the percentage of CO is higher than approx. 50% and 85% at 1 bar A and 5 bar A, respectively.

In the experiment, the range in the ratios of CO and CO_2 are given by (1) the lower limit of the evaporator used for the injection of steam with the reactant, and (2) setting the minimum flow higher than 10% of the capacity of the mass flow meters in the installation. Therefore, the ratios of CO : CO_2 were set at 0.2 : 0.8 and 0.7 : 0.3. In the example of a cell at thermodynamic equilibrium presented in the supplementary document, the second mixture coincides to an utilization factor of approximately 80% where the modular number is at the stochiometric value 3. However, at the outlet of the SOE, higher percentage of CO could occur at high utilization factor (> 80 %), where the PtM system would be at its highest efficiencies [5,6,50–53]. Consequently, the utilization factor of the SOE would be maximized which can result in CO percentages reaching above 80% where carbon formation is thermodynamically favored at the potential temperature level of the hot spot and within the operating pressure range of the reactor. Even though the ratios are limited to the region of unfavorable carbon deposition, for consistency with the operation of the SOE at high utilization factor and to avoid risk of carbon formation from local change in the composition, a ratio of H_2O :CO of 1 is maintained throughout the experiment.

The experiment design consists of an orthogonal matrix with two duplicates at the center and an extra point which differs from the duplicates by a single factor. The tested operating ranges of the various variables are presented in Table 1 with the justifications of each limit. In each case, the modular number of 3 was maintained; the stochiometric feed of H_2 to satisfy both overall reactions was injected.

The results are presented through the hydrogen dry concentration and methane yield. For direct-methane injection in the grid of Switzerland, a H_2 dry gas concentration under 5% is required, and H_2 is the limiting component when accounting for the stochiometric ratio between reactants. There is no measurement of flow rate at the outlet of the reactor, and the methane yields due to CO methanation and CO_2 methanation vary between points. Consequently, only the carbon to methane yield can be calculated based on the outlet's dry concentration:

$$Yield(\%) = \frac{CH_4^{out}}{CH_4^{out} + CO_2^{out} + CO^{out}} \tag{4}$$

Where the various concentrations are the dry concentration measured. Also, the inlet H/C ratio can be estimated:

$$H/C@inlet = \frac{8CH_4^{out} + 2H_2^{out}}{CH_4^{out} + CO_2^{out} + CO^{out}} \tag{5}$$

Where the values of 8 and 2 are the stochiometric ratios per H atom for the CO_2 methanation (and CO methanation with $1H_2O$/CO injected).

2.2. System simulation

The system simulation is performed with an in-house energy system integration platform, OSMOSE, using heat cascade calculations given

Table 1
Operating range.

Variables	Values	Justification
C flow [NL/min]	6	Designed nominal load reactant flow (approx. 3.8 kW HHV H2 SOE): GHSV = 1650/h with steam
	9	Higher load reactant flow (approx. 5.7 kW HHV H2 SOE): GHSV = 2480/h with steam
Ratio[CO:CO_2]	0.2: 0.8	Minimum CO for the stable and appropriate use of the evaporator
	0.7: 0.3	Minimum CO_2 is required to limit the error in the mass flow meter.
Water Pressure [bar A]	13	Minimize the risk of nickel tetracarbonyl formation [32] and ensure a minimum amount of reaction.
	15	Head limit of the make-up pump
Gas Pressure [barA]	4	Ensure a minimum kinetic for a hot spot to generate.
	6	Limited by the gas supply lines

Table 2
Operating variables for the system simulation.

Variables	Lower Bound	Upper Bound
SOE Inlet Temperature [° C]	680	
SOE outlet Modular number [-]	3.03	
SOE Pressure [bar A]	1.1	30
Oxygen Flow Rate [NmL/min/cm^2]	0	50
SOE Utilization Factor [%]	50	90
SOE current density [A/cm^2]	0.3	1.0
Evaporation Pressure [bar A]	1.1	30
Reactor Temperature [° C]	230	
Reactor Pressure [bar A]	1.1	30

minimum temperature difference of each heat stream. Thus, the simulation is the idealized case with no constraints on the number of heat exchanges. A multi-objective optimization scheme is used to guide the optimization towards the generation of Pareto Fronts: the optimal trade-off profile between two or three objectives. The platform first links the various Aspen plus models and runs them sequentially. The results such as the flow rates, temperature, pressure and heat duties are then extracted and the validity of the operating conditions are verified against user-defined constraints; in this analysis, a maximum temperature gradient in the stack of 120 °C is allowed. Finally, the objective functions are calculated and used for generating the set of operating variables.

The Aspen models are based on the work by Wang et al. [5,6,50–52] but with some alterations. The simplified PtM system simulated is presented in Fig. 4 with the various cases presented further. The recirculation of fuel is used to maintain a 10% H_2 at the inlet of the stack. An alternative operation of this unit is the possible pressurized evaporation independently of the stack pressure. A quasi 2D dusty gas model scheme was used to simulate the stack, and the calibration was performed in Wang et al. [5]. The stack model was calibrated using single cells and a short stack of 6 cells, all with the same composition. The fuel electrode is composed of nickel on porous yttria-stabilized zirconia (YSZ). The electrolyte is composed of 8 mol% (YSZ) and a gadolinium-doped ceria (GDC) layer between the YSZ and lanthanum strontium cobalt ferrite (LSCF) perovskite air electrode. The reactor is assumed to be an equilibrium reactor with the outlet following the equilibrium concentrations. All the compressors were multi-stage with inter-coolers, unless specified. The system capacity is dictated by a SOE stack of 80 cells of 80 cm^2. More details related to the stack models and solver can be found in the previous works [5,6,49–52]. The list of operating variables for both models with the allowable range is presented in Table 2.

CO methanation is more exothermal which helps satisfy the steam requirement by the SOE without using an external evaporator. However, there are multiple aspects that counter partially this gain, e.g.,

1. the SOE requires greater electrical power as CO_2 electrolysis is less efficient [41],
2. at ambient pressure, the CO_2 electrolysis and the reverse water gas shift (Eq. (3)) occurring in the presence of CO_2 and H_2 are endothermal while internal methanation occurring under pressurized operation is exothermal, affecting the thermal behavior of the stack and its integration in the system,
3. when performing CO methanation, it is recommended to inject steam to limit the risk off carbon deposition.

The effect of the last point on the system depends on the system layout. A list of system layout and how the steam requirement for CO methanation can impact the system are given below:

- Ambient SOE operation with separation of the steam at the outlet before compression: Steam would be injected before the methanation reactor, and thus, the total amount of steam required for the system would be similar to the steam electrolysis pathways followed by CO_2 methanation. This steam would require pressurized evaporation with a second evaporator or a single pressurized evaporation unit splitting of the generated steam.
- Ambient SOE operation without separation of the steam at the outlet before compression: The system's design becomes more complex (ex: compressor for a H_2, CO, CO_2, H_2O and CH_4 mixture) but the steam remaining at the outlet of the SOE can decrease (or even nullify) the need for a second steam injection in the system.
- Pressurization of the SOE with injection of the outlet gases into the reactor after cooling to the reactor's temperature: Pressurization of planar SOE have been performed only by a few [37–39,61] with multiple complications (leakages etc.). However, being able to inject directly without condensation allows the use of the steam at the outlet of the stack without the need of an adiabatic compressor. In addition, depending on the pressure level, as measured by Jensen et al. [39] and simulated by Wang et al. [5], even at high temperatures (700 °C and above), none negligible internal methanation can occur inside the stack. The methanation process releases steam that can then be re-electrolyzed, decreasing the steam required to be injected in the SOE. Wang et al. [5] identified an increase in efficiency at high utilization factor and lower current density due to pressurized operation with internal methanation.

The injection of steam at the inlet of the reactor requires a re-design of the system presented in Wang et al. [5] to either include a second steam generation unit (could be the same as the SOE's steam generation unit but with a second outlet) or the removal of the condensation process at the outlet of the SOE for the direct injection of the SOE product into the reactor (still requires a compressor as the reactor's pressure is

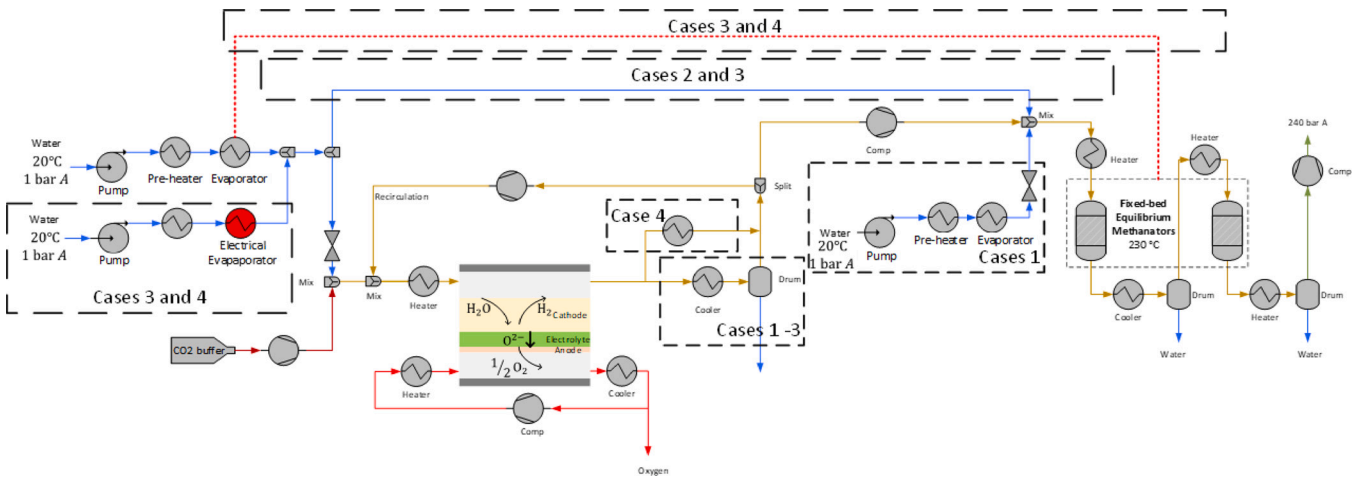

Fig. 4. SOE unit.
Source: Adapted from Aubin et al. [49] with permission from Elsevier, copyright 2023.

Table 3
Description of the four cases to be compared.

Cases	H_2O:CO ratio	Water at the SOE's outlet	Methanation unit's steam requirement details	Evaporation process
Ref.	0	Condensed and separated	None	No restriction in the number of evaporation process
1	1	Condensed and separated	Different SG than the SOE's SG with different allowed pressures	No restriction in the number of evaporation process
2	1	Condensed and separated	Same SG than the SOE's SG	No restriction in the number of evaporation process
3	1	Condensed and separated	Same SG than the SOE's SG	The reactor's cooling system only
4	1	Compressed with the syngas in a single-stage adiabatic compressor	Same SG than the SOE's SG	The reactor's cooling system only

higher than the stack pressure). In Fig. 4, the use of a different steam generation unit is shown by the extra evaporation process connected to the mixer located before the reactor. Conversely, the use of a same steam generation unit as the SOE is represented by the other connection onto the same mixer that originate before the SOE. In addition, as the simulation is idealized and only the heat cascade is assessed with no heat exchanger network included, the effect of the additional steam for the reactor can be different from the reality where the steam generation would come from a limited heat source: primarily the methanation heat generation process. This would result in the use of an electrical evaporator for compensation for any insufficient steam generation. Limiting the evaporation process to a single internal evaporator is shown in Fig. 4 by the red line that represents the heat supplied for the first evaporation coming from the reactor's heat production. The electrical evaporator is also presented in the figure when applicable (see Table 3). Therefore, the analysis presented below consists of the four different cases presented in Table 3.

In cases 3 & 4, when restricting the evaporation process to the reactor's cooling system, if the heat generated (minus the heat losses if included) is lower than the heat required to evaporated the steam, an external electrical evaporator is used to compensate as shown in Fig. 4. The last two cases are also simulated while considering a fix heat loss of 153 W estimated from the experimental results.

The comparison of the cases is based on the Pareto solutions (and front) generated from the multi-objectives optimization of both the methane flow rate leaving the system and the higher heating value (HHV) efficiency, the latter defined as:

$$\eta_{sys} = \dot{n}^{out}_{CH_4} HHV_{CH_4} / \dot{W}_{in}, \tag{6}$$

where $\dot{n}_{CH_4}$, HHV_{CH_4}, and $\dot{W}_{in}$ are the flow rate of methane produced, the higher heating values of methane, and the system's electrical input. Therefore, the optimization attempts at solving the overall objective function: Eq. (7).

$$Op = \min_{x \epsilon X}[-\dot{n}^{out}_{CH_4}(x), -\eta_{sys}(x)] \tag{7}$$

where x is a solution and X is the complete set of feasible solutions.

3. Results & discussion

3.1. Syngas methanation operation

3.1.1. Temperature profile

The temperature profiles measured along the reactor are grouped according to the percentage of CO and are presented in Fig. 5. Two pairs of points differing by only the $CO/(CO+CO_2)$ ratio injected are compared in Fig. 6: (a) a typical pair already at the inlet, and (b)

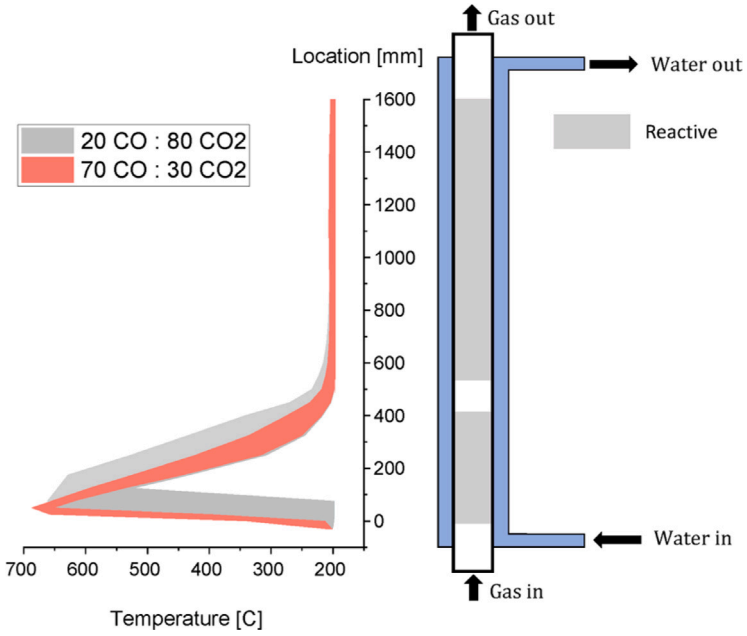

Fig. 5. Temperature profiles along the central axis of the reactor.

the pair of points with the largest change in the hot spot profile. The increase in the $CO/(CO+CO_2)$ ratio of the injected gas causes the profiles for all the cases with higher CO percentage to move closer to the inlet while their hot spots are higher. Within each group, higher reactant pressure, higher cooling water pressure and lower flow rates cause the hot spot to be closer to the inlet.

For all the pairs of points differing by only the $CO/(CO+CO_2)$ ratio, the measured hot spot temperature increase is between 18.8 and 49 °C, from approx. 627–661 °C to 655–688 °C. However, the largest increase in the measured hot spot is caused by the finite number of measurement locations. The shift in the location of the hot spot varies significantly between the pairs. For one group of pairs, mostly the low reactant flow rates, the hot spot is already rigidly located at the inlet, as presented by the case with the smallest change, and thus, increasing the CO percentage did not shift the hot spot. Conversely, for the higher reactant flow rate and low pressures, the hot spot at 20% CO is further up the reactor. This is the result of the inlet being relatively low in temperature; the rate of reaction does not excessively surpass the cooling. Examining the case with the largest change, over the first 75–100 mm, the temperature at the center of the reactor is slightly decreasing, however, the overall rate of reaction accounts for the entirety of the radial profile. Therefore, it is proposed that once the radial temperature profile is high enough, the reaction overcomes the cooling and the temperature rapidly increases. The higher exothermicity of the CO methanation could be adding the required heat to overcome the cooling from the start of the reactor which results in the hot spot of the lowest pressures and highest reactant flow rate to shift by 7–10 cm to reach the entrance of the reactor when 70% of the carbon is injected as CO. Conversely, as mentioned in the introduction, CO can hinder CO_2 methanation, and thus, with higher concentration of CO, the activation of the CO_2 methanation could occur further from the start of the reactive zone.

The addition of steam at the inlet decreases the magnitude of the hot spot through two mechanisms: (1) an increase in convection and (2) a decrease in kinetics through the increase in the partial pressure of one of the products. As the outlet temperature is dictated by the cooling water pressure in addition to having similar gas composition at the outlet, all the outlet temperatures are similar regardless of their inlet composition. However, the interaction of the steam with the injected CO could affect the local temperature profile. Even though the amount of H_2 required for the reaction decreases as the CO is increased, the space velocity is maintained constant as steam is injected. In their experiment, Mebrahtu et al. [7] measured a decrease in CH_4 selectivity (increase in CO_2 selectivity) with the increased percentage of CO in the presence of steam that resulted in a net WGS reaction. Consequently, at the inlet of the reactor, the injected steam could react with the CO, which is in relatively high concentration, to form H_2 and CO_2 which is favored at the inlet's temperature. The WGS is exothermal and thus could further ensure sufficient heat at the inlet to bring the hot spot closer to the inlet. However, the hot spot is higher than the temperature at which a net RWGS should be observed. Further investigation would be required to measure the extent of the WGS reaction between the inlet and the hot spot. However, depending on the extent, it would help explain the trend in the magnitude of the hot spot.

Operating a reactor designed for CO_2 methanation with syngas (or CO) emphasized the concern related to hot spot control. A reactor with a slightly smaller diameter would be favored for such operation. The increase in flow velocity would push the hot spot towards the outlet while decreasing its magnitude by reducing the bed's thermal resistance. The decrease in the hot spot decreases risk of degradation of the pellets thermally in addition to moving away from the operating region where carbon deposition occurs. This would allow a decrease in the steam injected with the reactant. If less or no steam is injected with the reactant; the steam requirement of the complete system (SOE + methanation) can be decreased. However, the increase in the reaction's kinetic and a decrease in convection from the removal of the steam would lead to a higher spot located closer to the inlet, and thus, the diameter would have to be further decreased.

The formation of carbonyl with the higher CO concentration and low temperature is assumed negligible because the minimum temperature is 10 s of degrees above the onset of thermal decomposition of the molecule. However, some formation could still take place which would accelerate the deactivation of the catalyst at the inlet where the temperature is still low and the concentration is high. On the other side of the hot spot, the RWGS and CO methanation should have caused the concentration to decrease significantly.

No consensus exists on the exact phase the temperature measurement using the thermocouple represents: solid [62] or gas [63]. However, as mentioned by Aubin et al. [49], there can also be some axial conduction in the thermocouple that generates a discrepancy between

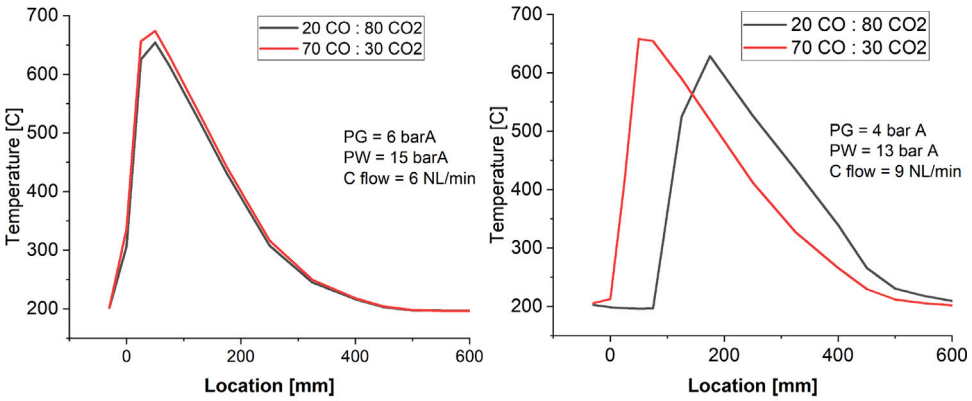

(a) Typical Pair with hot spot close to the inlet **(b)** Pair with the largest change in the hot spot

Fig. 6. Two pairs of operating points: the smallest and largest changes in the profiles as the CO percentage increases.

the measured value and the bed or gas phase temperature. Therefore, at the hot spot, the temperature at the catalyst might differ from the measured value, and a long term test would have to be performed to verify the degradation of the hot spot by identifying: (1) any drift in the hot spot location, and (2) any drop in outlet conversion.

3.1.2. H_2 concentration and methane yield

With the ratio of C/H/O injected, it can be assumed that carbon formation is negligible. In Figs. 7, the results of the analysis are presented as the mean values with the measurement error represented as a standard deviation range. In addition, the arrows link the pairs of points differing by only the focused variable of each graph. For direct injection into the gas grid, the limit of H_2 concentration varies significantly between the countries [64]. The PtM system under development is to be operated in Switzerland with a 5% limit, and thus, within the current operating range of the reactor, the dry gas concentrations are still above the limit.

In Fig. 7, as it was observed in the case of CO_2 methanation, increases in both the gas pressure and cooling water pressure decrease the H_2 dry gas concentration. The improvement of the H_2 concentration with the increase in gas pressure and cooling water pressure would be the result of the same effects that caused the higher hot spot: the raise in the reactions kinetics. For the reaction pressure, it is the consequence of the volume reduction of the methanation process. As for the cooling water pressure, the resulting rise in the minimum temperature in the reactor improves the overall kinetics since the overall reaction has yet to reach equilibrium. Similarly, the decrease in carbon flow rate (and the related decrease in total flowrate) lowers the H_2 concentration at the outlet of the reactor due to the higher residence time. Consequently, while maintaining the modular number at 3, to reach the limit for direct injection into the gas grid, the gas pressure and/or water pressure would have to be increased further, and/or the reactant flow rate would have to be reduced. Alternatively, as it was done in the previous publication [49] with CO_2 methanation, an small excess of CO_2 (or CO) could be injected which could help the H_2 conversion while still being under the 4% limit in CO_2 required. However, with any modification, the hot spot would have to be further investigated to ensure the stability of pellets at an even higher hot spot.

At the outlet, the CO concentration for all of the operating points was below 1%, which could be explained by: (1) CO methanation can have higher kinetics [28], and/or (2) the reverse-water-gas-shift favors the formation of CO_2 through the excess steam, and/or (3) as it was described in the previous section, the suppression of the CO_2 methanation. Even if at the hot spot, the temperature is high enough for the equilibrium to favor significant CO production, as the temperature decreases, the conversion of CO would be prioritized. Nevertheless, on a macro level, when focusing on the effect of the percentage of C injected as CO, the effect depends on the total quantity of reactant. The extra mole of H_2 required for the methanation of CO_2 can result in a larger quantity of H_2 at the outlet depending on the reaction rate difference between the two methanation reactions.

However, the observation indicates an opposite response in H_2 concentration when increasing the CO percentage between lower and higher total carbon flow rate. At higher flow rates, increasing the CO percentage brings the temperature closer to the inlet, and thus, decreases the potential quench effect of the second injection's inert region. However, Fig. 8 presents both the hydrogen concentration and methane yield with color mapping based on the estimated H/C ratio at the inlet. The H_2 concentration is still primarily dictated by the total flow rate of reactant. However, the relative change in H_2 concentration for each pair of points whose only difference is the total flow rate of reactant is affected by the H/C ratio. The increase in H_2 concentration between group 1, and group 2 is different than the difference between group 3 and group 4 while the change in H/C is opposite between the groups.

In the case of the methane yield, the mapping suggests that the H/C ratio is the primary cause for the trend. At lower CO percentage, an increase in total flow rate caused an increase in H/C ratio and an increase in methane yield. The opposite trend in the methane yield occurs at higher CO percentage. The effect of the CO percentage could be hidden by this more significant effect. Even the equilibrium concentration is affected by the actual H/C/O ratios injected as shown in Fig. 9. The cases with the addition or subtraction of 1% of the injected CO differs in equilibrium H_2 concentration by more than a percent. Therefore, if the ratio H/C/O is not 8/1/2, the outlet concentration can differ significantly.

3.1.3. Steam generation

During the experiment, the steam generation was estimated using the make-up pump flow meter with a correction from the water level in the separator. However, some points might still have some transient behavior and some variables, affecting the quantity of heat available, not linked to the reaction might also differ slightly between points. These can cause variations and uncertainties in the gain in steam generation from CO_2 methanation to CO methanation. If we omit the outliers (points 1 and 2) of Fig. 10, there is an increase in steam generation between 7 and 11% between the pairs of points with only the percentage of CO changing from 20 to 70%. Based on the enthalpy changes at 200 °C (the outlet of the reactor) and the change in CO percentage, the potential gain in heat produced is approximately 11%. In Aubin et al. [49], the authors identified a heat exchanger efficiency between 80 and 89% for the equivalent CH_4 production

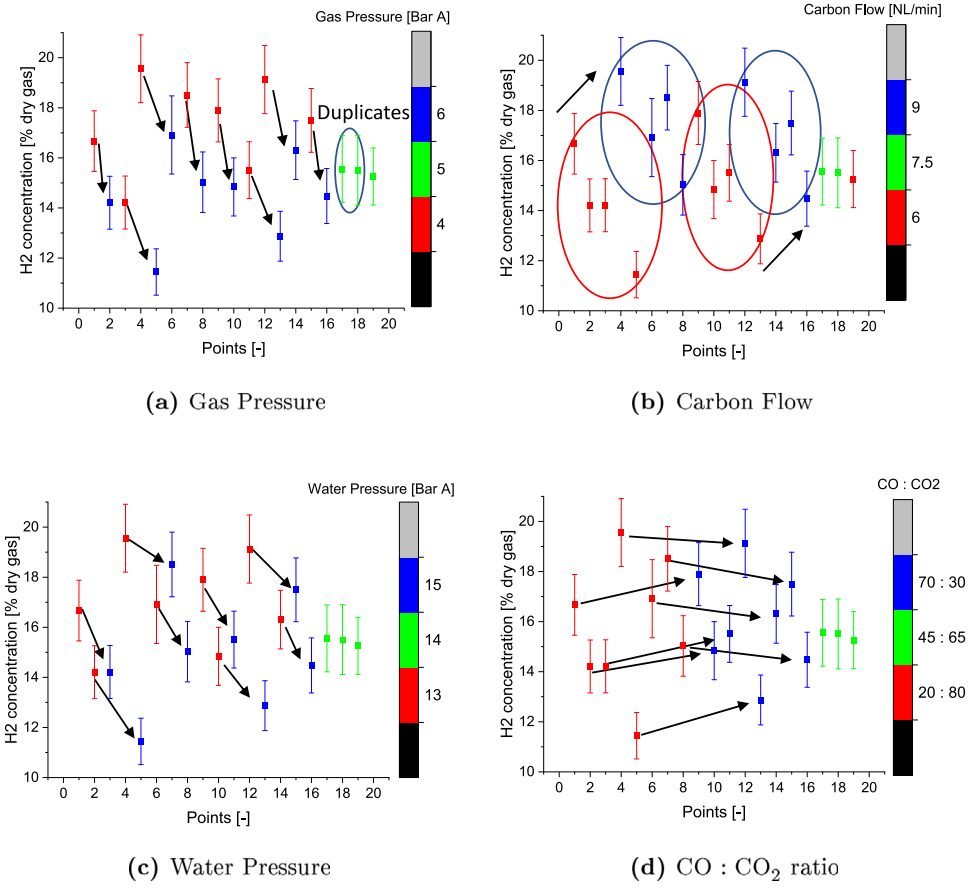

(a) Gas Pressure (b) Carbon Flow

(c) Water Pressure (d) CO : CO_2 ratio

Fig. 7. H_2 concentration at the outlet of the reactor for all the operating points, and with the four main control variables.

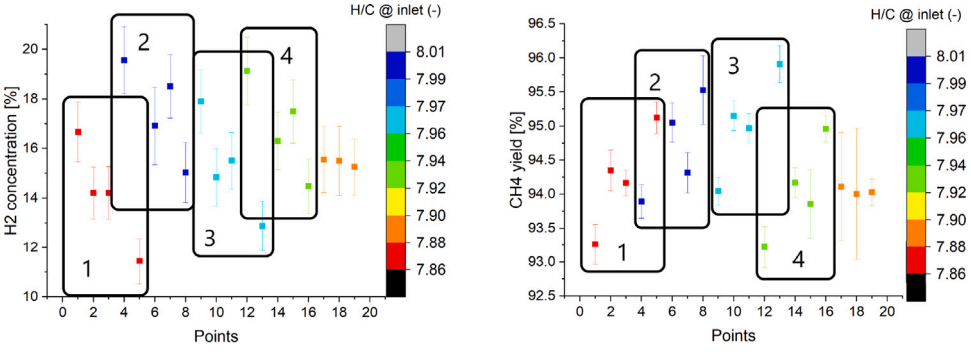

(a) H_2 concentration (b) Methane Yield

Fig. 8. H_2 concentration (a) and methane yield (b) for all the operating points as a function of the estimated C/H ratio.

during pure CO_2 methanation. Therefore, the results gathered during syngas methanation are in accordance with the results in pure CO_2 methanation.

On the other hand, the injection of steam with a ratio of 1 H_2O/CO causes an increase in the steam requirement of the system. Depending on the layout of the system (avoiding the separation of the steam after the SOE, and the introduction of a second evaporation process using hot flows of the system) and the system's operating conditions (steam utilization in the SOE, pressurized evaporation etc.), the addition of the injected steam can outweigh the potential gain in the steam generated in the reactor during syngas methanation. Consequently, a system analysis is needed to verify the impact of CO methanation while avoiding the risks of carbon deposition through steam injection. Increasing the CO injection from 20% to 70% implies an increase in steam requirement of 0.15 and 0.22 kg/h for 6 NL/min and 9 NL/min of carbon injected, respectively. Depending on the evaporation pressure, the heat required to evaporate the steam injected in the reactor as a percentage of the additional heat generated varies; at 15 bar A, 86.8% of the theoretical increase in heat generated is used. Furthermore, when accounting for conversion and heat losses, the percentage can reach above 100%. Nevertheless, according to the thermodynamic equilibrium, the ratio of 1 H_2O/CO is highly conservative, and thus removing part of the injected steam could ensure that the gain in steam generation will be lower than the steam injected. In addition, the improved kinetic with the reduction of the quantity of steam injected would improve the conversion and yield through the removal of a product, and thus, the steam generation would increase.

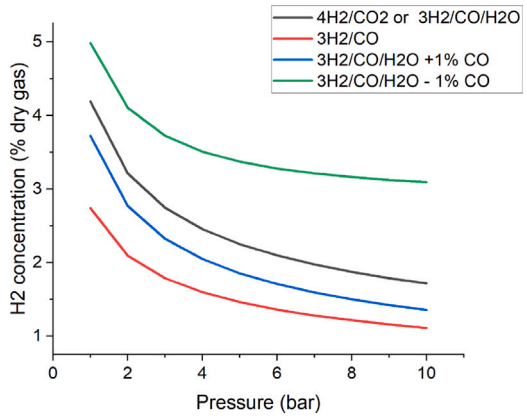

Fig. 9. Equilibrium concentration at 200 °C as a function of pressure for CO methanation and CO_2 methanation (or CO with 1 H_2O/CO) in addition to H_2/CO/H_2O +/- 1% CO.

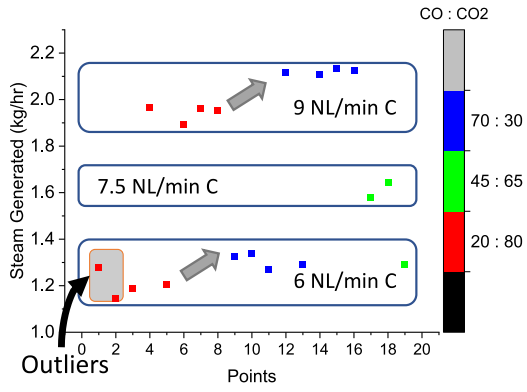

Fig. 10. Steam generation.

3.2. System analysis

The Pareto solutions for the reference case are presented in the supplementary document as it is a re-assessment of the analysis presented in previous work [5,6,50,52] but with an emphasis of certain aspects relevant to the comparison with the alternatives cases.

The alternative cases consider the required steam injection in the reactor with a steam to CO ratio of at least 1: the minimum ratio recommended by the manufacturer. The comparison of the cases are based on the effect on the Pareto front (Fig. 11) and (2) the modification of the operating conditions along the front (Fig. 12). For reason of clarity and conciseness, the Grand Composite Curve at 4 yields along the Pareto Front for each case are presented and analyzed in the supplementary document. Similarly, the operating maps for some of the operating variables for the 4 sets of Pareto solutions are also provided in the supplementary document. Nevertheless, numerical instabilities in multi-variable systems limit the generation of general claims during the analysis of sets of Pareto solutions as multiple combinations of variables can provide the same response. The comparison of the Pareto fronts indicate primarily a shift of the best efficiency at the lowest loads and at the highest loads towards lower efficiencies for the last two cases. However, the profile of the operating variables along the Pareto fronts varies between each cases; also indicating the multitude of combinations that can result in efficiencies close to the front.

Comparing case 1 (original layout with the added reactor steam requirement provided by a second steam generation process) with the original (without steam requirement) shows limited impact of adding a second steam requirement since the system is idealized and the pressure of the steam injected in the reactor is allowed to be different from the primary steam generation. Consequently, the system operated the second evaporator at a lower temperature level such that the flows requiring to be cooled (outlet of SOE and outlet of reactor) can be used to evaporate the reactor's required steam input. The operating conditions of this case versus the original case do not differ significantly as there is sufficient heat at the various levels to generate the additional steam; the profiles of the operating variables displayed on Fig. 12 are almost identical.

When enforcing the reactor's steam generation to the same evaporation process than the SOE's steam generation unit (Case 2), with the same evaporating pressure for both the SOE's and methanator's steam generation process, the response exhibits almost the same Pareto front as Case 1. Nevertheless, the front at higher yield is composed of operating conditions that should be found slightly under the Pareto front of case 1: at a higher utilization factor and observed in Fig. 12. This can be seen on the complete operating map comparison presented in the supplementary document. On the Pareto solutions of case 1, at higher yield, points with slightly higher utilization than the points on the front have marginally lower HHV efficiency. The evaporating plateau on the GCC getting longer for the same set of operation conditions (RU etc.), results in the RU being maintained slightly higher to avoid the formation of a pinch. At higher current density, the cell is highly exothermal, and thus, there is sufficient heat to evaporate the entirety of the steam required, and thus, the RU can be minimized to improve the stack performance. The idealization of the system and the limited stress Case 2's conditions add to the system results in a small increase in the RU at higher yield. However, as shown on the operating conditions at the Pareto front (Fig. 12), and on the GCC presented in the supplementary document, the set of solutions indicate an upward shift in the water pressures, just under the formation of a pinch. Increasing the pressure decreases the latent heat which limits the need to increase the utilization factor.

When enforcing that the reactor's cooling system is the only internal evaporator (Case 3), the system response indicates more significant changes in the operating conditions. First, the Pareto front is shifted to the left at a location where the operation allows the internal thermal integration to satisfy completely the steam generation without requiring an external evaporation process, as shown by the minimization of the evaporation power required on Fig. 12 (C). On Fig. 12, as internal methanation removes potential heat generation in the reactor, lower stack pressure operation is favored even at lower yield compared to previous cases. The evaporation pressure, however, is maintained higher to ensure lower latent heat. For the entire set of Pareto solutions, the utilization factor is also increased. At high yield, the constant utilization factor line at the higher yield portion of the front is no longer close to the lower limit but is now slightly higher in amplitude and is no longer constant; bringing the front slightly lower in efficiency. The increase in utilization factor is to avoid the use of the external evaporator that induces even greater losses in the system's efficiency. Consequently, the selection of the stack pressure, evaporation pressure and the utilization factor is based on minimizing the need for an external evaporator without causing additional losses. Furthermore, this trade-off is not only identified for the Pareto front but for the entire set of Pareto solutions presented in the supplementary document.

When avoiding the condensation at the outlet of the SOE (Case 4), the impacts of the increase in steam demand and the limitation to a single internal evaporator are reduced. The Pareto front partially shifts back towards values similar to the original case. At lower yield, pressurized operation and internal methanation is again maximized, while the utilization factor at higher yield is decreased to improve the stack performance. The GCC of this case is not presented as it does not differ significantly from the GCC of Case 3. The removal of the condensation stage, separation stage and the modification from a multi-stage inter-cooled compressor to a compressor suited for compressing humid mixtures can change the system's response regardless of the steam requirement in the reactor. Therefore, the referenced Pareto front

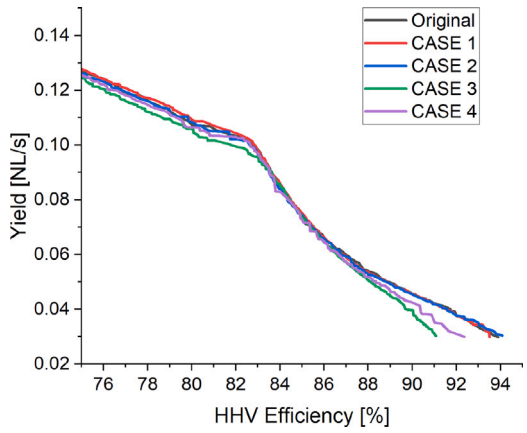

Fig. 11. Pareto front comparison of the original case and the cases 1 to 4.

would thus be slightly different for the two layouts, either in location or in operating conditions. In the location of the inflation point, the significant decrease coincides with the decreases in utilization factor and reactor pressure At higher yield, the reactor pressure differs between the two cases, but due to the limited change, the comparison is provided in the supplementary document.

The results of stressing the system further by including heat losses in the reactor is presented in Fig. 13 by comparing cases 3 and 4, the only internal steam generation process is the reactor's cooling system, and with or without condensing and separating the water at the outlet of the SOE, respectively. The use of excess steam at the inlet of the reactor, compared to the requirement from thermodynamics, caused the removal of the condensation and separation steps to be favored as it is less affected by the heat losses in the system. This is represented by the lower increase in utilization factor in the SOE when including heat loss in the reactor as shown in Fig. 14 (c).

3.2.1. Discussion

The selections of the final layout and of the operating strategy is a multifaceted process that need to consider: (1) the cost, (2) the technological challenges, (3) the degradation, and (4) the performance. As the quantitative assessment of the first 3 points are beyond the scope of this study, here are some brief qualitative remarks that were identified:

1. The selection of the layout and operating strategy would have to account for degradation as the degradation rate could vary between operating points.
2. The cost gain or loss of restricting the amount of evaporation process would depend on the relative saving of the extra heat exchanger design for two-phase heat transfer and the possible cost of the extra evaporator. The design of the realized reactor presented in this manuscript allows the use of external heating, installed for the start-up of the reactor, for compensation if needed, avoiding the need of an external evaporator.
3. The compression unit for humid mixtures would require significant heating to avoid condensation in the compressor and in any buffer tanks used to avoid instantaneous vacuum in the SOE when the compressor is started. Consequently, this layout is more technologically challenging and might be costlier.

Concentrating on the instant performance, the idealization of the system through omitting the losses in the SOE and in the BoP, and only considering the heat cascade, limits the impact the cases have on the location of the Pareto front. However, some portions of the Pareto front did experience noticeable shift. In addition, the modifications of the operating variables to maintain the highest efficiency possible provides important conclusions to be drawn for the system layout and the operating strategy:

1. Operating variables, mainly the SOE pressure, and responses, such as the SOE outlet temperature, affect the available heat for steam production. In this example, the SOE pressure and outlet temperature dictate the amount of internal methanation which shifts a portion of the heat generation from the reactor to the stack. This results in a larger amount of heat unavailable for the steam generation if the SOE's outlets are not included in the steam generation process. Consequently, in addition to cost and technological challenges that were mentioned above, the selection of the layout should also depend on the purpose of the system: maximizing methane formation in the SOE followed by methane upgrading would require the use of the SOE's outlet enthalpy to complete the steam production, or operate at lower internal methanation with higher load for the methanation process.
2. The RU at the front is selected to satisfy the heat integration by avoiding the formation of a pinch while maximizing the stack performance provided by lower RU. The locations at the front that experienced a pinch were affected by the increase in steam requirement but most significantly by restricting the evaporation process. Therefore, the effect of the RU on the stack performance becomes less important than its effect on the steam requirement. Conversely, the effect of the water pressure is very volatile due to the limited cost of pressurizing water. Two instants were observed where the water pressure was restricted: (1) at low yield, the water pressure needs to increase as the SOE pressure also increases, and (2) the water pressure can be maximized if the decrease in the latent heat of evaporation benefits the thermal management. A consequence of the design of the reactor is the requirement for pressurized evaporation in the cooling system. According to the system simulation, the water pressure used in the reactor should have limited impact on the system's performance as the reactor temperature is always higher than its cooling system's temperature; no cross over can occur.
3. Regardless of the level of idealization of the simulation, while still omitting losses, the results showed a decrease in HHV efficiency between cases 2 and 3 of approx. 3.0%, 0%, and 0.8% points at 0.03, 0.075, and 0.15 NL/s of CH_4 produced, respectively, compared to only 1.7%, 0% and 0.4% point between cases 2 and 4. Interestingly, around where the nominal production would be located, the effect of the layout is negligible and has similar operating variables.
4. The effect of accounting for the heat losses can spread the Pareto fronts of cases 3 and 4 around the nominal operating conditions and at higher yield. The largest difference between case 3 (with condensation) and case 4 (without condensation) occurs around the nominal production (about 0.063NL/s CH_4) with case 4 having the higher efficiency by approx. 1.2% point.

As such a system can be used at a fixed load or with varying load (ex: storing excess production of variable sources of renewable electricity), the system's operating strategy and optimal layout could vary with the intended load profile. An example of the effect of the load profile on the selection of the layout and operating strategy is the distribution of the risk of carbon deposition in the reactor with the operation of the SOE. As it was discussed in the methodology, carbon formation can occur in the dry gas leaving the SOE once injected in the reactor if the C:O and C:H ratios exceed a threshold depending on the pressure and hot spot temperature. However, with the CO_2 injected, the risk of carbon deposition decreased significantly. Pressurizing the reactor to 5 bar A would already avoid carbon formation for mixtures with $CO/(CO+CO_2)$ ratios of less than approx. 85%, which can, depending on the stack operating conditions, be above a reactant utilization factor of 90%. Consequently, the steam requirement to avoid carbon deposition would also depend on the load at which the system is operated at. If at part load and under pressurized SOE, the methanation reactor can be itself

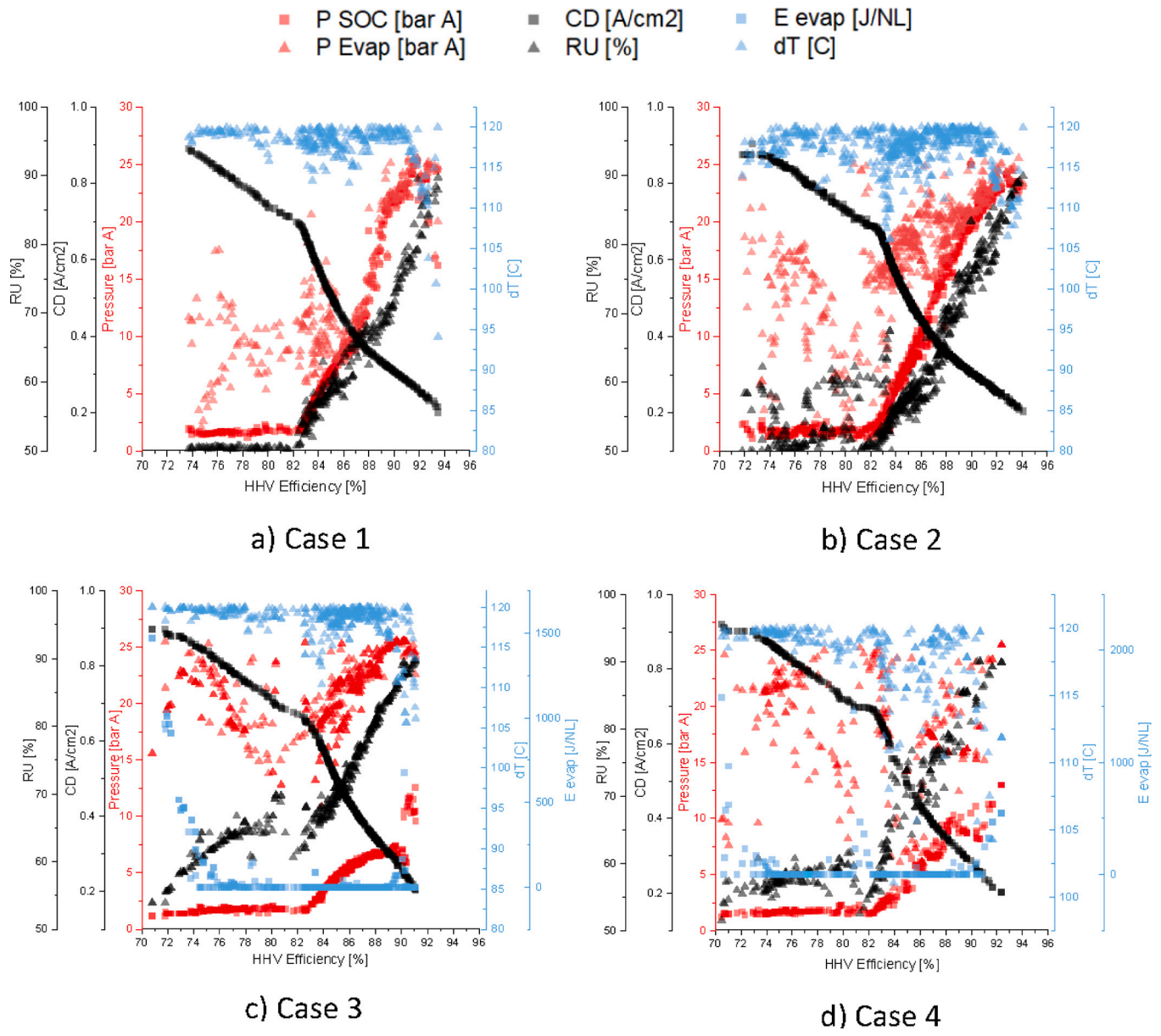

Fig. 12. Comparison of the variables at the Pareto front for the 4 different cases.

pressurized without requiring a compressor between the units, then the additional steam generation could be avoided. Similarly, at high load, according to the simulation, the RU drops drastically such that a very light compression of the dry gas for the methanation reactor would be enough to avoid the formation of carbon deposition. Conversely, in partial load and nominal load while operating the SOE in the state-of-the-art conditions, at ambient pressure, the high utilization factor and potentially low reactor pressure could thermodynamically favor carbon formation at the temperature of the reactor's hot spot. As a result, the selection between condensing and not condensing the outlet of the SOE before the compressor would depend on the load profile. Furthermore, the analysis of the idealized system already indicates a drop in the maximum efficiency of the system when the evaporation process is limited to a single evaporator. This deficiency is exacerbated by including heat losses inside the reactor. However, these losses should not scale linearly with the system's capacity, and thus, the results should shift towards the ideal case with system size.

The operation in co-electrolysis followed by syngas methanation is a valid operating mode that ideally allows for better thermal integration occurring under pressurized operation. However, the performance of the simulation is affected by the layout as presented, but also through the selection of operating variables and idealized components. The injection of steam should also affect the conversion inside the reactor. The use of an equilibrium reactor does not capture this behavior. In the final system, the Pareto front at higher yield would be negatively affected by not removing the steam after the reactor as the ratio of steam to CO reaches values far above 1, potentially decreasing the conversion. To compensate, a larger reactor would have to be used to ensure sufficient conversion over the entire range of operating conditions.

Furthermore, restricting the number of evaporators limits the system's capacity to be pressurized and perform internal methanation. Consequently, a system with the majority of the methane being generated in the SOE, that would coincide thermodynamically with high pressure (above 30 bar A) and low temperatures (below 600 °C), would require the SOE to be included in the steam generation process. Such integration could be completed either through using the sweep air to evaporate steam which would increase the flow rate required and decrease the overall efficiency or through novel heat extraction process, such as high temperature heat pipes.

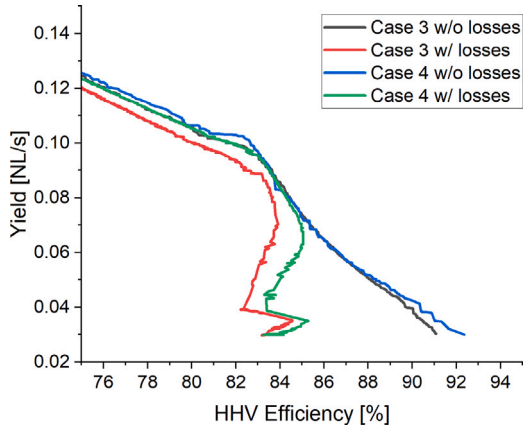

Fig. 13. Pareto front for cases 3 and 4 with and without 153 W of heat losses in the reactor.

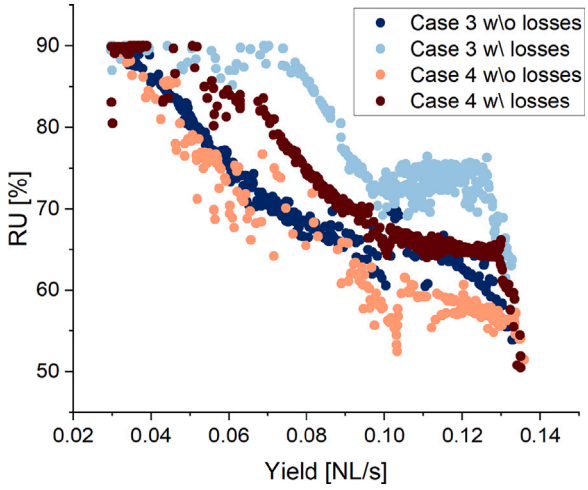

Fig. 14. Reactant utilization factor along the Pareto fronts presented in Fig. 13.

Nevertheless, the simulated cases represent extreme cases in which the steam injected is over twice the quantity needed to avoid carbon formation according to thermodynamic calculation minimizing the Gibbs free energy. Consequently, once a typical load profile has been selected, and the performance of the methanation reactor over its operating range has been mapped, the assessment could be expanded to include a heat exchanger network design and the methanation reactor's conversion measurement.

4. Conclusions

Syngas (or CO) methanation causes an increase in the magnitude of the measured hot spot by 19–49 °C by increasing the CO:CO_2 ratio from 0.2:0.8 to 0.7:0.3. As was the case for CO_2 methanation, increasing both the gas pressure and the cooling water pressure improves the yield and conversion of the reactor. Yet, the H_2 concentration ranges between 10.5 and 20.1% which is still above the current 5 % limit for direct injection in the grid of Switzerland. Potentially due to the errors in the reactant injected in the reactor, the effect of total reactant flow rate and the effect of the carbon injected in the form of CO vs. CO_2 cannot be fully captured. Injecting steam to avoid deposition is an effective method which has limited impact on the theoretical efficiency of an idealized system. Even when the system is strained by forcing a single internal evaporation process, the increase in steam requirement alters the Pareto front negligibly at around the nominal load while a drop of up to 3% points was observed at partial load. The modifications are dictated by the thermal integration: (1) the stack no longer reaches the same maximum pressure as internal methanation removes heat generation in the reactor (the only source of heat for the steam generation), and (2) the front located at higher yield is composed of higher utilization factor as the gain in stack performance is less than the cost of evaporating a greater excess. The conclusion of the system analysis is limited by assuming an idealized system with an infinite number of heat exchangers and no heat loss. When simulating a system without the condensation and separation of the steam at the outlet of the SOE, the Pareto front is improved partially towards the case with unlimited evaporators (+1.3% point at maximum efficiency compared to case 3) as the excess steam ensures the minimum ratio of steam to CO to be injected in the reactor. In addition, this layout is less affected by heat losses in the reactor compared to the case with condensation and separation. The inclusion of a fixed heat exchanger network would provide additional insight in the impact of additional steam requirement to avoid carbon deposition. Lastly, the selection between condensation or the omission thereof at the outlet of the SOE is also dependent on the load profile, cost and technical limitations, which will be considered when designing the final realized system.

CRediT authorship contribution statement

Philippe Aubin: Conceptualization, Methodology, Visualization, Software, Investigation, Writing – original draft. **Ligang Wang:** Software, Supervision, Writing – original Draft. **Jan Van herle:** Funding acquisition, Supervision, Writing – review & editing.

Declaration of competing interest

The authors declare the following financial interests/personal relationships which may be considered as potential competing interests: Jan Van herle reports financial support was provided by Gaznat SA. Jan Van herle reports financial support was provided by Swiss Federal Office of Energy. Jan Van herle reports equipment, drugs, or supplies was provided by Hitachi Zosen Inova AG. Jan Van herle reports financial support was provided by European Union Horizon 2020. Ligang Wang reports financial support was provided by National Natural Science Foundation of China. Ligang Wang reports financial support was provided by Interdisciplinary Innovation Program of North China Electric Power University.

Data availability

The data that has been used is confidential.

Acknowledgments

This research was funded by the HOTCAT4STEAM project from the Swiss Federal Energy Office, by the European Union's Horizon 2020 under grant agreements n. 731224 (BALANCE, topic LCE-33-2016), by GAZNAT in the scope of a project on the development of a SOE-methanation coupling, and by the EPFL-Wallis and HES-SO joint Valais demonstrator. The authors would like to thank Hitachi Zosen for supplying the catalyst. The National Nature Science Foundation of China (Grant No. 52090062, 52276186) and Interdisciplinary Innovation Program of North China Electric Power University provided fundings to the author L. Wang.

Appendix A. Supplementary data

Supplementary material related to this article can be found online at https://doi.org/10.1016/j.enconman.2023.117520.

References

[1] Rönsch S, Schneider J, Matthischke S, Schlüter M, Götz M, Lefebvre J, et al. Review on methanation – From fundamentals to current projects. Fuel 2016;166:276–96. http://dx.doi.org/10.1016/j.fuel.2015.10.111, URL https://www.sciencedirect.com/science/article/pii/S0016236115011254.

[2] Pattabathula V, Richardson J. Introduction to ammonia production. Chem Eng Prog 2016;112(9):69–75.

[3] Ren J, Liu Y-L, Zhao X-Y, Cao J-P. Methanation of syngas from biomass gasification: An overview. Int J Hydrogen Energy 2020;45(7):4223–43. http://dx.doi.org/10.1016/j.ijhydene.2019.12.023, URL https://www.sciencedirect.com/science/article/pii/S0360319919345239.

[4] Nguyen T, Wissing L, Skjøth-Rasmussen M. High temperature methanation: Catalyst considerations. Catal Synth Fuels State Art Outlook 2013;215:233–8. http://dx.doi.org/10.1016/j.cattod.2013.03.035, URL https://www.sciencedirect.com/science/article/pii/S0920586113001491.

[5] Wang L, Rao M, Diethelm S, Lin T-E, Zhang H, Hagen A, et al. Power-to-methane via co-electrolysis of H2O and CO2: The effects of pressurized operation and internal methanation. Appl Energy 2019;250:1432–45. http://dx.doi.org/10.1016/j.apenergy.2019.05.098, URL https://www.sciencedirect.com/science/article/pii/S0306261919309493.

[6] Wang L, Zhang Y, Pérez-Fortes M, Aubin P, Lin T-E, Yang Y, et al. Reversible solid-oxide cell stack based power-to-x-to-power systems: Comparison of thermodynamic performance. Appl Energy 2020;275:115330. http://dx.doi.org/10.1016/j.apenergy.2020.115330, URL https://www.sciencedirect.com/science/article/pii/S0306261920308424.

[7] Mebrahtu C, Nohl M, Dittrich L, Foit SR, de Haart LGJB, Eichel R-A, et al. Integrated co-electrolysis and syngas methanation for the direct production of synthetic natural gas from CO2 and H2O. ChemSusChem 2021;14(11):2295–302. http://dx.doi.org/10.1002/cssc.202002904, Publisher: John Wiley & Sons, Ltd.

[8] Gao J, Wang Y, Ping Y, Hu D, Xu G, Gu F, et al. A thermodynamic analysis of methanation reactions of carbon oxides for the production of synthetic natural gas. RSC Adv 2012;2(6):2358–68. http://dx.doi.org/10.1039/C2RA00632D.

[9] Fisher IA, Bell AT. A comparative study of CO and CO2hydrogenation over Rh/SiO2. J Catalysis 1996;162(1):54–65. http://dx.doi.org/10.1006/jcat.1996.0259, URL https://www.sciencedirect.com/science/article/pii/S0021951796902596.

[10] Park J-N, McFarland EW. A highly dispersed Pd–Mg/SiO2 catalyst active for methanation of CO2. J Catalysis 2009;266(1):92–7. http://dx.doi.org/10.1016/j.jcat.2009.05.018, URL https://www.sciencedirect.com/science/article/pii/S0021951709001754.

[11] Weatherbee GD, Bartholomew CH. Hydrogenation of CO2 on group VIII metals: II. Kinetics and mechanism of CO2 hydrogenation on nickel. J Catalysis 1982;77(2):460–72. http://dx.doi.org/10.1016/0021-9517(82)90186-5, URL https://www.sciencedirect.com/science/article/pii/0021951782901865.

[12] Osaki T, Mori T. Kinetic studies of CO2dissociation on supported Ni catalysts. React Kinetics Catal Lett 2005;87(1):149–56. http://dx.doi.org/10.1007/s11144-006-0020-8.

[13] Ashok J, Ang M, Kawi S. Enhanced activity of CO2 methanation over Ni/CeO2-ZrO2 catalysts: Influence of preparation methods. In: Special issue on the XIII international conference on carbon dioxide utilization, vol. 281. 2017;304–11. http://dx.doi.org/10.1016/j.cattod.2016.07.020, URL https://www.sciencedirect.com/science/article/pii/S0920586116304850.

[14] Jia X, Zhang X, Rui N, Hu X, Liu C-j. Structural effect of Ni/ZrO2 catalyst on CO2 methanation with enhanced activity. Appl Catal B 2019;244:159–69. http://dx.doi.org/10.1016/j.apcatb.2018.11.024, URL https://www.sciencedirect.com/science/article/pii/S0926337318310749.

[15] Takano H, Shinomiya H, Izumiya K, Kumagai N, Habazaki H, Hashimoto K. CO2 methanation of Ni catalysts supported on tetragonal ZrO2 doped with Ca2+ and Ni2+ ions. Int J Hydrogen Energy 2015;40(26):8347–55. http://dx.doi.org/10.1016/j.ijhydene.2015.04.128, URL https://www.sciencedirect.com/science/article/pii/S0360319915010666.

[16] Aldana PU, Ocampo F, Kobl K, Louis B, Thibault-Starzyk F, Daturi M, et al. Catalytic CO2 valorization into CH4 on Ni-based ceria-zirconia. Reaction mechanism by operando IR spectroscopy. Catal Synth Fuels State Art Outlook 2013;215:201–7. http://dx.doi.org/10.1016/j.cattod.2013.02.019, URL https://www.sciencedirect.com/science/article/pii/S0920586113000874.

[17] Köck E-M, Kogler M, Bielz T, Klötzer B, Penner S. In situ FT-IR spectroscopic study of CO2 and CO adsorption on Y2O3, ZrO2, and Yttria-stabilized ZrO2. J Phys Chem C 2013;117(34):17666–73. http://dx.doi.org/10.1021/jp405625x, Publisher: American Chemical Society.

[18] Pokrovski K, Jung KT, Bell AT. Investigation of CO and CO2 adsorption on tetragonal and monoclinic zirconia. Langmuir 2001;17(14):4297–303. http://dx.doi.org/10.1021/la001723z, Publisher: American Chemical Society.

[19] Bachiller-Baeza B, Rodriguez-Ramos I, Guerrero-Ruiz A. Interaction of carbon dioxide with the surface of zirconia polymorphs. Langmuir 1998;14(13):3556–64. http://dx.doi.org/10.1021/la970856q, Publisher: American Chemical Society.

[20] Solis-Garcia A, Louvier-Hernandez JF, Almendarez-Camarillo A, Fierro-Gonzalez JC. Participation of surface bicarbonate, formate and methoxy species in the carbon dioxide methanation catalyzed by ZrO2-supported Ni. Appl Catal B 2017;218:611–20. http://dx.doi.org/10.1016/j.apcatb.2017.06.063, URL https://www.sciencedirect.com/science/article/pii/S0926337317306069.

[21] Ashok J, Pati S, Hongmanorom P, Tianxi Z, Junmei C, Kawi S. A review of recent catalyst advances in CO2 methanation processes. VSI: EurasiaCat 2020;356:471–89. http://dx.doi.org/10.1016/j.cattod.2020.07.023, URL https://www.sciencedirect.com/science/article/pii/S0920586120304880.

[22] Schmider D, Maier L, Deutschmann O. Reaction kinetics of CO and CO2 methanation over nickel. Ind Eng Chem Res 2021;60(16):5792–805. http://dx.doi.org/10.1021/acs.iecr.1c00389.

[23] Zhao K, Li Z, Bian L. CO2 methanation and co-methanation of CO and CO2 over Mn-promoted Ni/Al2O3 catalysts. Front Chem Sci Eng 2016;10(2):273–80. http://dx.doi.org/10.1007/s11705-016-1563-5.

[24] Kokka A, Ramantani T, Petala A, Panagiotopoulou P. Effect of the nature of the support, operating and pretreatment conditions on the catalytic performance of supported Ni catalysts for the selective methanation of CO. SI: Energy Environ 2020;355:832–43. http://dx.doi.org/10.1016/j.cattod.2019.04.015, URL https://www.sciencedirect.com/science/article/pii/S0920586119301634.

[25] Inul T, Funabiki M, Takegami Y. Simultaneous methanation of CO and CO2 on supported Ni-based composite catalysts. Ind Eng Chem Prod Res Dev 1980;19(3):385–8. http://dx.doi.org/10.1021/i360075a018, Publisher: American Chemical Society.

[26] Le TA, Kim MS, Lee SH, Kim TW, Park ED. CO and CO2 methanation over supported Ni catalysts. In: Special issue of international symposium on catalytic conversion of energy and resources, vol. 293–294. 2017;89–96. http://dx.doi.org/10.1016/j.cattod.2016.12.036, URL https://www.sciencedirect.com/science/article/pii/S0920586116308550.

[27] Jaworski Z, Pianko-Oprych P. A comparative thermodynamic study of equilibrium conditions for carbon deposition from catalytic C–H–O reformates. Energies 2018;11(5). http://dx.doi.org/10.3390/en11051177.

[28] Miao B, Ma SSK, Wang X, Su H, Chan SH. Catalysis mechanisms of CO2 and CO methanation. Catal Sci Technol 2016;6(12):4048–58. http://dx.doi.org/10.1039/C6CY00478D, Publisher: The Royal Society of Chemistry.

[29] McCarty J, Wise H. Hydrogenation of surface carbon on alumina-supported nickel. J Catalysis 1979;57(3):406–16. http://dx.doi.org/10.1016/0021-9517(79)90007-1, URL https://www.sciencedirect.com/science/article/pii/0021951779900071.

[30] Barrientos J, Gonzalez N, Boutonnet M, Järås S. Deactivation of Ni/γ-Al2O3 catalysts in CO methanation: Effect of Zr, Mg, Ba and Ca oxide promoters. Top Catalysis 2017;60(17):1276–84. http://dx.doi.org/10.1007/s11244-017-0812-2.

[31] Li W, Nie X, Jiang X, Zhang A, Ding F, Liu M, et al. ZrO2 support imparts superior activity and stability of Co catalysts for CO2 methanation. Appl Catal B 2018;220:397–408. http://dx.doi.org/10.1016/j.apcatb.2017.08.048, URL https://www.sciencedirect.com/science/article/pii/S0926337317307841.

[32] Pedersen K, Skov A, Rostrup-Nielsen JR. Catalytic aspects of high temperature methanation. Am Chem Soc, Div Fuel Chem, Prepr; (United States) 1979;25:2. URL https://www.osti.gov/biblio/5235839.

[33] Timmermann H, Sawady W, Reimert R, Ivers-Tiffée E. Kinetics of (reversible) internal reforming of methane in solid oxide fuel cells under stationary and APU conditions. J Power Sources 2010;195(1):214–22. http://dx.doi.org/10.1016/j.jpowsour.2009.07.019, URL https://www.sciencedirect.com/science/article/pii/S0378775309011975.

[34] Zeng H, Wang Y, Shi Y, Cai N, Yuan D. Highly thermal integrated heat pipe-solid oxide fuel cell. Appl Energy 2018;216:613–9. http://dx.doi.org/10.1016/j.apenergy.2018.02.040, URL https://www.sciencedirect.com/science/article/pii/S030626191830165X.

[35] Biswas S, Kulkarni AP, Giddey S, Bhattacharya S. A review on synthesis of methane as a pathway for renewable energy storage with a focus on solid oxide electrolytic cell-based processes. Front Energy Res 2020;8. URL https://www.frontiersin.org/articles/10.3389/fenrg.2020.570112.

[36] Sun X, Chen M, Jensen SH, Ebbesen SD, Graves C, Mogensen M. Thermodynamic analysis of synthetic hydrocarbon fuel production in pressurized solid oxide electrolysis cells. HySafe 1 2012;37(22):17101–10. http://dx.doi.org/10.1016/j.ijhydene.2012.08.125, URL https://www.sciencedirect.com/science/article/pii/S0360319912019751.

[37] Bernadet L, Gousseau G, Chatroux A, Laurencin J, Mauvy F, Reytier M. Influence of pressure on solid oxide electrolysis cells investigated by experimental and modeling approach. Int J Hydrogen Energy 2015;40(38):12918–28. http://dx.doi.org/10.1016/j.ijhydene.2015.07.099, URL https://www.sciencedirect.com/science/article/pii/S0360319915019023.

[38] Bernadet L, Laurencin J, Roux G, Montinaro D, Mauvy F, Reytier M. Effects of pressure on high temperature steam and carbon dioxide Co-electrolysis. Electrochim Acta 2017;253:114–27. http://dx.doi.org/10.1016/j.electacta.2017.09.037, URL https://www.sciencedirect.com/science/article/pii/S0013468617319084.

[39] Jensen SH, Langnickel H, Hintzen N, Chen M, Sun X, Hauch A, et al. Reversible operation of a pressurized solid oxide cell stack using carbonaceous gases. J Energy Storage 2019;22:106–15. http://dx.doi.org/10.1016/j.est.2019.02.003, URL https://www.sciencedirect.com/science/article/pii/S2352152X18307941.

[40] Riedel M, Heddrich M, Friedrich K. Investigation of the long-term stability of solid oxide electrolysis stacks under pressurized conditions in exothermic steam and Co-electrolysis mode. Fuel Cells 2020;20(5):592–607. http://dx.doi.org/10.1002/fuce.202000011.

[41] Riedel M, Heddrich M, Ansar A, Fang Q, Blum L, Friedrich K. Pressurized operation of solid oxide electrolysis stacks: An experimental comparison of the performance of 10-layer stacks with fuel electrode and electrolyte supported cell concepts. J Power Sources 2020;475:228682. http://dx.doi.org/10.1016/j.jpowsour.2020.228682, URL https://www.sciencedirect.com/science/article/pii/S0378775320309861.

[42] Wu P, Shy S. Cell performance, impedance, and various resistances measurements of an anode-supported button cell using a new pressurized solid oxide fuel cell rig at 1–5 atm and 750–850 °C. J Power Sources 2017;362:105–14. http://dx.doi.org/10.1016/j.jpowsour.2017.07.030, URL https://www.sciencedirect.com/science/article/pii/S0378775317309126.

[43] Baxter SJ, Rine M, Min B, Liu Y, Yao J. Near 100% CO2 conversion and CH4 selectivity in a solid oxide electrolysis cell with integrated catalyst operating at 450C. J CO2 Util 2022;59:101954. http://dx.doi.org/10.1016/j.jcou.2022.101954, URL https://www.sciencedirect.com/science/article/pii/S2212982022000737.

[44] Du Y, Qin Y, Zhang G, Yin Y, Jiao K, Du Q. Modelling of effect of pressure on co-electrolysis of water and carbon dioxide in solid oxide electrolysis cell. Int J Hydrogen Energy 2019;44(7):3456–69. http://dx.doi.org/10.1016/j.ijhydene.2018.12.078, URL https://www.sciencedirect.com/science/article/pii/S0360319918340424.

[45] Fujiwara N, Tada S, Kikuchi R. Power-to-gas systems utilizing methanation reaction in solid oxide electrolysis cell cathodes: a model-based study. Sustain Energy Fuels 2020;4(6):2691–706. http://dx.doi.org/10.1039/C9SE00835G.

[46] Chen B, Xu H, Ni M. Modelling of SOEC-FT reactor: Pressure effects on methanation process. Appl Energy 2017;185:814–24. http://dx.doi.org/10.1016/j.apenergy.2016.10.095, URL https://www.sciencedirect.com/science/article/pii/S0306261916315422.

[47] Chen Y, Luo Y, Shi Y, Cai N. Theoretical modeling of a pressurized tubular reversible solid oxide cell for methane production by co-electrolysis. Appl Energy 2020;268:114927. http://dx.doi.org/10.1016/j.apenergy.2020.114927, URL https://www.sciencedirect.com/science/article/pii/S0306261920304396.

[48] Kazempoor P, Braun R. Hydrogen and synthetic fuel production using high temperature solid oxide electrolysis cells (SOECs). Int J Hydrogen Energy 2015;40(9):3599–612. http://dx.doi.org/10.1016/j.ijhydene.2014.12.126, URL https://www.sciencedirect.com/science/article/pii/S0360319914035605.

[49] Aubin P, Wang L, Van herle J. Evaporating water-cooled methanation reactor for solid-oxide stack-based power-to-methane systems: Design, experiment and modeling. Chem Eng J 2022;140256. http://dx.doi.org/10.1016/j.cej.2022.140256, URL https://www.sciencedirect.com/science/article/pii/S1385894722057369.

[50] Wang L, Chen M, Küngas R, Lin T-E, Diethelm S, Maréchal F, et al. Power-to-fuels via solid-oxide electrolyzer: Operating window and techno-economics. Renew Sustain Energy Rev 2019;110:174–87. http://dx.doi.org/10.1016/j.rser.2019.04.071, URL https://www.sciencedirect.com/science/article/pii/S1364032119302928.

[51] Wang L, Pérez-Fortes M, Madi H, Diethelm S, herle JV, Maréchal F. Optimal design of solid-oxide electrolyzer based power-to-methane systems: A comprehensive comparison between steam electrolysis and co-electrolysis. Appl Energy 2018;211:1060–79. http://dx.doi.org/10.1016/j.apenergy.2017.11.050, URL http://www.sciencedirect.com/science/article/pii/S0306261917316367.

[52] Wang L, Düll J, Maréchal F, Van herle J. Trade-off designs and comparative exergy evaluation of solid-oxide electrolyzer based power-to-methane plants. Special Issue Power Gas Hydrog Appl Energy Syst Diff Scales - Build Dist Natl Lev 2019;44(19):9529–43. http://dx.doi.org/10.1016/j.ijhydene.2018.11.151, URL https://www.sciencedirect.com/science/article/pii/S0360319918337832.

[53] Jeanmonod G, Wang L, Diethelm S, Maréchal F, Van herle J. Trade-off designs of power-to-methane systems via solid-oxide electrolyzer and the application to biogas upgrading. Appl Energy 2019;247:572–81. http://dx.doi.org/10.1016/j.apenergy.2019.04.055, URL https://www.sciencedirect.com/science/article/pii/S0306261919307020.

[54] Vágner P, Kodým R, Bouzek K. Thermodynamic analysis of high temperature steam and carbon dioxide systems in solid oxide cells. Sustain Energy Fuels 2019;3(8):2076–86. http://dx.doi.org/10.1039/c9se00030e.

[55] Stoots C, O'Brien J, Hartvigsen J. Results of recent high temperature coelectrolysis studies at the Idaho National Laboratory. Int J Hydrogen Energy 2009;34(9):4208–15. http://dx.doi.org/10.1016/j.ijhydene.2008.08.029, URL https://www.sciencedirect.com/science/article/pii/S0360319908009932.

[56] Ioannidou E, Neophytides S, Niakolas D. Experimental clarification of the RWGS reaction effect in H2O/CO2 SOEC co-electrolysis conditions. Catalysts 2019;9(2). http://dx.doi.org/10.3390/catal9020151.

[57] Li Q, Zheng Y, Sun Y, Li T, Xu C, Wang W, Chan SH. Understanding the occurrence of the individual CO2 electrolysis during H2O-CO2 co-electrolysis in classic planar Ni-YSZ/YSZ/LSM-YSZ solid oxide cells. Electrochim Acta 2019;318:440–8. http://dx.doi.org/10.1016/j.electacta.2019.06.108, URL https://www.sciencedirect.com/science/article/pii/S0013468619312514.

[58] Yoon S-E, Song S-H, Choi J, Ahn J-Y, Kim B-K, Park J-S. Coelectrolysis of steam and CO2 in a solid oxide electrolysis cell with ceramic composite electrodes. Int J Hydrogen Energy 2014;39(11):5497–504. http://dx.doi.org/10.1016/j.ijhydene.2014.01.124, URL https://www.sciencedirect.com/science/article/pii/S0360319914002043.

[59] Graves C, Ebbesen SD, Mogensen M. Co-electrolysis of CO2 and H2O in solid oxide cells: Performance and durability. In: Proceedings of the 17th international conference on solid state ionics, vol. 192, no. 1. 2011, p. 398–403. http://dx.doi.org/10.1016/j.ssi.2010.06.014, URL https://www.sciencedirect.com/science/article/pii/S0167273810003188.

[60] Qi H, Zhang J, Tu B, Yin Y, Zhang T, Liu D, et al. Extreme management strategy and thermodynamic analysis of high temperature H2O/CO2 co-electrolysis for energy conversion. Renew Energy 2022;183:229–41. http://dx.doi.org/10.1016/j.renene.2021.10.096, URL https://www.sciencedirect.com/science/article/pii/S0960148121015627.

[61] Clausen LR, Butera G, Jensen SH. High efficiency SNG production from biomass and electricity by integrating gasification with pressurized solid oxide electrolysis cells. Energy 2019;172:1117–31. http://dx.doi.org/10.1016/j.energy.2019.02.039, URL https://www.sciencedirect.com/science/article/pii/S0360544219302282.

[62] Zhang W, Machida H, Takano H, Izumiya K, Norinaga K. Computational fluid dynamics simulation of CO2 methanation in a shell-and-tube reactor with multi-region conjugate heat transfer. Chem Eng Sci 2020;211:115276. http://dx.doi.org/10.1016/j.ces.2019.115276, URL https://www.sciencedirect.com/science/article/pii/S0009250919307663.

[63] Schlereth D, Hinrichsen O. A fixed-bed reactor modeling study on the methanation of CO2. In: ECCE9 – 9th European congress of chemical engineering, vol. 92, no. 4. 2014;702–12. http://dx.doi.org/10.1016/j.cherd.2013.11.014, URL https://www.sciencedirect.com/science/article/pii/S0263876213005054.

[64] EBA, MARCOGAZ, editors. Biomethane: responsibilities for injection into natural gas grid. Technical Association of the European Gas Industry (MARCOGAZ); 2019, URL https://www.marcogaz.org/wp-content/uploads/2021/04/WG_GQ-237.pdf.